Composite Structures 313 (2023) 116927

Contents lists available at ScienceDirect

Composite Structures

journal homepage: www.elsevier.com/locate/compstruct

Supersonic flutter of variable stiffness circular cylindrical shells

Duarte Cachulo[1], Hamed Akhavan[2], Pedro Ribeiro[3,*]

INEGI/DEMec, Faculdade de Engenharia, Universidade do Porto, Porto, 4200-465, Portugal

ARTICLE INFO

Keywords:
Flutter
Circular cylindrical shells
Composite
Curvilinear fibres
p-version finite element method

ABSTRACT

Curvilinear reinforcement fibres allow to tailor the elastic properties of composite laminates in space, leading to Variable Stiffness Composite Laminates (VSCL). In this work, the aeroelastic stability of VSCL cylindrical shells under a supersonic airflow along the axial direction is analysed in order to verify if curvilinear fibres can be used to increase the flutter speed. A linear mathematical model for thin circular cylindrical VSCL shells is developed for that purpose. The aerodynamic pressure caused by the supersonic airflow is modelled recurring to the linearised piston theory. The *p*-version of the finite element method is used to transform the differential equations of motion from partial to ordinary. Using the latter, eigenvalue problems are defined to obtain the natural frequencies and mode shapes of vibration, and the critical flutter conditions. Various types of curvilinear fibre paths are explored, to find paths that result in higher values of critical flutter free stream pressure. The values are compared with the ones of conventional, constant stiffness, composite laminated shells.

1. Introduction

Fibre reinforced composite laminates are used in various industries due to advantageous material properties, which include high stiffness and strength-to-weight ratios [1]. Another advantage of these materials is that designers can select the fibre directions and the layup in order to approach desired properties. In comparison to the more traditional straight fibres, curvilinear fibres increase the level of design flexibility, enabling enhanced tailoring towards the loads that the structure is expected to withstand. Laminated shells with curvilinear fibres can be designated as variable stiffness composite laminated (VSCL) shells. They find potential application in the aeronautic industry, where high ratio between stiffness and weight is crucial. Examples include parts of the fuselages of aircraft and rockets. Here, the study of flutter is important, as this aeroelastic instability may result in damage or catastrophic failure [2]. Considering this, a question arises: can the implementation of variable stiffness properties on composite laminated shells improve the mechanical performance against aeroelastic flutter? The present work has the goal of helping to answer this question. Specifically, this paper addresses the aeroelastic flutter phenomenon caused by an axial airflow at supersonic speed, along the external surface of a variable stiffness composite laminate, thin, circular cylindrical shell.

Since curvilinear fibres can be used to achieve a composite material with advantageous properties, various authors have addressed this type of composites. Efforts have been made to exploit the design possibilities [3–5], to deal with challenges in the design and optimisation [3,5] and with issues related to manufacturing processes [6–8]. As these review papers show, the justified interest in VSCLs led to a large number of publications; for the sake of conciseness, the following paragraphs only mention publications directly related to the topics of this paper: VSCL cylindrical shells, aeroelastic problems in VSCLs, flutter on closed cylindrical shells in other materials. By "closed" it is meant that the cross section contains a full circle.

One of the first analysis on VSCL shells was presented by Tatting [9], who explored the effectiveness of the variable stiffness concept when applied to cylindrical shells. Governing equations were derived, buckling was analysed, optimisation methods applied and attention was given to the Brazier effect. Blom et al. [10,11] optimised the fundamental frequency of vibration and the buckling response of VSCL cylinders. Blom et al. [10–12] also addressed the influence of tow-drop areas, gaps and overlaps, on the stiffness and strength of VSCL shells. ABAQUS was employed in [10–12]. Wu et al. [13,14] and Pan et al. [15] addressed the design of VSCL shells, with particular consideration given to manufacturing aspects of the process. Furthermore, in [16], Wu et al. carried out a structural assessment of VSCL shells resorting to experimental and analytical methods. Nik [17] optimised VSCL structures (mostly plates, but cylindrical shells are also addressed), to maximise buckling

* Corresponding author.
E-mail addresses: dcachulo@inegi.up.pt (D. Cachulo), hakhavan@inegi.up.pt (H. Akhavan), pmleal@fe.up.pt (P. Ribeiro).
[1] Postmaster researcher.
[2] Postdoctoral researcher.
[3] Associate professor.

https://doi.org/10.1016/j.compstruct.2023.116927
Received 24 November 2022; Received in revised form 3 March 2023; Accepted 14 March 2023
Available online 16 March 2023

Nomenclature

Latin Letters

a_∞	Speed of sound
E_{ii}	Young's moduli
f_r	Shape function along the ξ coordinate, for transverse displacement w_0
$\mathbf{ff_u}$, $\mathbf{ff_v}$, $\mathbf{ff_w}$	Shape function vectors for u_0, v_0 and w_0 displacement components
G_{12}	Shear modulus
g_r	Shape function along the ξ coordinate, for membrane displacements
g_{ur}, g_{vr}	Shape functions along the ξ coordinate, for membrane displacements u_0 and v_0
h_{ur}, h_{vr}, h_{wr}	Shape functions along the θ coordinate, for displacement u_0, v_0 and w_0
h	Cylindrical shell's thickness
$\mathbf{K}$	Stiffness matrix
k_{xx}, $k_{\theta\theta}$	Shell's change of curvature in the polar coordinate system
$k_{x\theta}$	Shell's twist in the polar coordinate system
l	Cylindrical shell's length
$\mathbf{M}$	Mass matrix
M_{ij}	Internal moment resultants per unit length
M	Mach number
m	Number of axial waves for free vibration/flutter modes
$\mathbf{N}$	Shape function matrix
N_{ij}	Internal force resultants per unit length
n	Number of circumferential waves for free vibration/flutter modes
n_{crit}	Number of circumferential waves of the first mode that achieves flutter
$\mathbf{p}$	External pressure vector
p_∞	Free stream static pressure
p_a	Aerodynamic pressure
p_{crit}	Critical flutter free flow static pressure
p_m, p_o, p_t	Number of shape functions used from the g, f and h sets of shape functions
p_{tot}	Total number of degrees of freedom
$\mathbf{q}$	Coefficient vector for stability analysis
$\mathbf{q_t}$	Generalised coordinates vector
R	Shell's middle surface radius
r_ψ	Fibre path turning radius
t	Time variable
u, v, w	Displacement components along the x, θ and z coordinates
u_0, v_0, w_0	Middle surface displacement components along the x, θ and z coordinates
v_{ij}	Poissons ratio's
x, θ, z	Cylindrical coordinates

Greek Letters

ϵ_{ij}	Components of strain tensor
γ	Air's specific heat ratio
γ_{ij}	Engineering shear strains
ψ	Fibre ply angle
ρ	Material volumetric mass density
ρ_{fluid}	Fluid volumetric mass density
σ_{ij}	Components of stress tensor
ξ	Adimensional axial coordinate
ω_i	Natural frequency of vibration of the i^{th} mode
Ω	Eigenvalue in aeroelastic problems

load and in-plane stiffness, where manufacturing induced defects were considered. Rouhi et al. [18] manufactured a VSCL cylindrical shell and tested it for buckling conditions. An improvement in the buckling load was achieved using curvilinear fibres, compared to a quasi-isotropic counterpart. Labans and Bisagni [19] carried out numerical analysis and experimental tests to determine buckling and vibration modes of VSCL shells. Almeida et al. [20] presented a methodology to optimise VSCL cylindrical shells under axial compression, using an optimisation concept based on the manufacturing characteristics of the Tailored Fibre Placement process; post-buckling was also analysed.

In [21], the modes of vibration of VSCL open, cylindrical, shallow shells were studied in the linear regime, using a *p*-version of the finite element type model. In a follow up, the non-linear modes were analysed [22]. Both in [21,22], the curvature of the shell's middle surface led curvilinear fibres to have consequences not found in modes of vibration of plates. Ritz-based procedures - which can be considered to be a *p*-version finite element type method [23] - have been applied to analyse VSCL shells, requiring far fewer degrees of freedom than procedures based on *h*-version type finite elements [24–26]. Multi-part structural geometries were represented as an assembly of shell-like domains. With this approach, Sciascia et al. investigated the natural modes of vibration, buckling modes, linear transient and dynamic stability of general VS doubly-curved shells, with and without prestress [24–26].

Some works - Refs. [27–35] - have been published on aeroelastic instability of VSCL plates. The latter group of references addressed supersonic flutter and divergence on VSCL plates by the *p*-version FEM, from the linear to the non-linear regimes. In [36], aeroelastic instabilities of hybrid composite laminated plates with carbon nanotubes and curvilinear fibres are investigated.

Supersonic flutter on isotropic, closed, cylindrical shells has been analysed in diverse publications, including [37–43], mostly reviewed in Chapter 15 of [44]. Mentioning just the more recent of those references, Amabili and Pellicano [42] considered imperfections of the geometry of the cylindrical shells and showed it has an effect on flutter onset; a multi-degree of freedom model was employed and non-linear oscillations studied. Sabri and Lakis [43] presented a finite element method based on Sander's shell theory, with fast convergence to analyse circular cylindrical shells subjected to external supersonic flow.

Flutter of non-isotropic and/or non-homogeneous closed circular cylindrical shells has also been analysed. The effects of temperature, damping and geometric properties on the flutter stability of sandwich shells were studied in [45]. Chen and Li [46] studied flutter onset and the ensuing limit cycles on composite laminated cylindrical shells. Avramov et al. [47] studied the limit cycle oscillations of cylindrical shells reinforced by carbon nanotubes and under a supersonic flow. The aeroelastic stability of axially functionally graded cylindrical shells is investigated in [48], it is proposed to add a lumped mass to eliminate the mode coalescence associated with flutter.

In spite of the potential of VSCL for aeronautic applications, aeroelastic supersonic instabilities on variable stiffness composite laminated cylindrical shells have not yet, to the best of the authors knowledge, been studied. This is the topic of analysis of the present article. In Section 2, the equations of motion for a thin circular cylindrical shell are established based on Love's first approximation assumptions. The linear model is then implemented recurring to a *p*-version finite element method (*p*-FEM), which is also described. The aerodynamic forces created by the axial airflow at supersonic speeds are modelled using

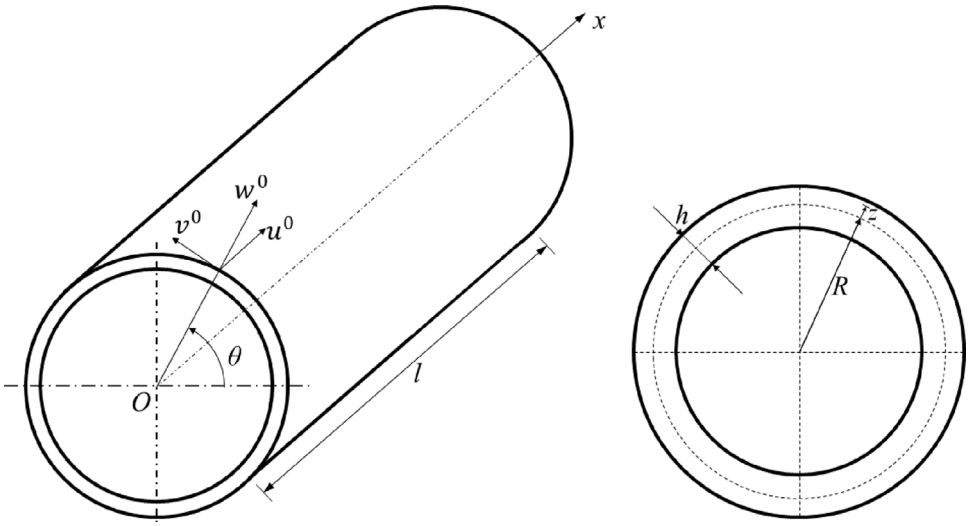

Fig. 1. Cylindrical shell dimensions, coordinate system and displacement components (perspective and cross sectional views).

the linear piston theory with a correction factor to account for the curvature, then the calculation of the critical free stream pressure for the occurrence of flutter can be made. In Section 3, a convergence test is presented and the model is verified. In Section 4, curvilinear fibre paths that, in comparison to unidirectional fibre paths, increase the value of the free stream static pressure at which flutter occurs are searched for. Finally, Section 5 concludes the paper.

2. Mathematical model

In this section, the linear model for thin variable stiffness composite laminated circular cylindrical shells under an axial supersonic airflow is presented. Since the analysis addresses critical flutter speeds, not the ensuing oscillations, a linear model suffices [2]. According to [1], a shell can be considered as thin if, in the limit (Qatu writes "probably smaller for composite materials"), the thickness is smaller than $(1/20)^{\text{th}}$ of the smallest wave length of the motion and/or radii of curvature of the shell. Only very thin shells will be analysed in this work, so that a thin shell model provides a reasonable approximation. Axial variation of stiffness is considered, with fibre paths shifting along the circumferential direction. Gaps and overlaps in the fibre distribution [49,50] and geometric imperfections may significantly affect the vibrations of circular cylindrical shells [44,51]; however, in this first work imperfections are not considered. Piston theory was chosen to model the pressure due to the supersonic axial airflow, because it provides useful insights, is relatively straightforward and has a low computational cost [2,52]. Naturally, the aeroelastic model cannot be used in the subsonic and transonic regimes.

The relevant dimensions, the coordinate system and the components of displacement of points on the middle surface are represented in Fig. 1.

Love's first approximation hypotheses [53] are considered. This enables the elasticity problem to be reduced from a 3D to a 2D problem by considering that the strains in each point of the body can be expressed as a function of strains and curvature changes on the middle surface. This simplification allows the derivation of Eqs. (1)

$$\epsilon^0_{xx} = \frac{\partial u_0}{\partial x} \tag{1a}$$

$$\epsilon^0_{\theta\theta} = \frac{1}{R}\frac{\partial v_0}{\partial \theta} + \frac{w_0}{R} \tag{1b}$$

$$\gamma^0_{x\theta} = \frac{1}{R}\frac{\partial u_0}{\partial \theta} + \frac{\partial v_0}{\partial x} \tag{1c}$$

$$k_{xx} = -\frac{\partial^2 w_0}{\partial x^2} \tag{1d}$$

$$k_{\theta\theta} = \frac{1}{R^2}\frac{\partial v_0}{\partial \theta} - \frac{1}{R^2}\frac{\partial^2 w_0}{\partial \theta^2} \tag{1e}$$

$$k_{x\theta} = \frac{1}{R}\frac{\partial v_0}{\partial x} - \frac{2}{R}\frac{\partial^2 w_0}{\partial x \partial \theta} \tag{1f}$$

which are valid for the specific case of cylindrical shells (page 262 of [1]).

A composite laminated shell is composed of several layers. In each layer, constant stiffness composite laminates maintain a constant tow angle ψ, whereas in variable stiffness composite laminates the tow angle varies along the spacial coordinates. Four types of curvilinear fibre paths are considered here: linear angle variation paths with 1 segment, constant in-plane curvature (in this article, "in-plane" refers to the surface obtained by extending the shell over one plane) path with 1 segment, linear angle variation paths with 2 segments and constant in-plane curvature path with 2 segments. These are respectively defined by mathematical expressions dependent on parameters T_0 and T_1, seen in Eqs. (2)–(5) and are schematically represented in Fig. 2. The ξ coordinate is used as an adimensional axial coordinate that varies between -1 and 1 and that relates to the x coordinate as $x = \frac{l}{2}\cdot(\xi+1)$. Throughout this work, the notation $\langle T_0, T_1\rangle$ is used to refer to a linear angle variation path with one segment; $\langle T_0, T_1\rangle_c$ is used to refer to a constant in-plane curvature path with one segment, $\langle T_1, T_0, T_1\rangle$ is used to refer to a linear angle variation path with two segments and $\langle T_1, T_0, T_1\rangle_c$ is used to refer to a constant in-plane curvature path with two segments.

$$\psi(\xi) = (T_1 - T_0)\cdot\frac{\xi+1}{2} + T_0 \tag{2}$$

$$\psi(\xi) = \arcsin\left\{\sin(T_0) + [\sin(T_1) - \sin(T_0)]\cdot\frac{\xi+1}{2}\right\} \tag{3}$$

$$\psi(\xi) = (T_1 - T_0)\cdot|\xi| + T_0 \tag{4}$$

$$\psi(\xi) = \arcsin\left\{\sin(T_0) + [\sin(T_1) - \sin(T_0)]\cdot|\xi|\right\} \tag{5}$$

For the constitutive model, a relation between the force and moment resultants and the strain components can be established, giving rise to expression (6).

$$\begin{Bmatrix} N_{xx} \\ N_{\theta\theta} \\ N_{x\theta} \\ M_{xx} \\ M_{\theta\theta} \\ M_{x\theta} \end{Bmatrix} = \begin{bmatrix} A_{11} & A_{12} & A_{16} & B_{11} & B_{12} & B_{16} \\ A_{12} & A_{22} & A_{26} & B_{12} & B_{22} & B_{26} \\ A_{16} & A_{26} & A_{66} & B_{16} & B_{26} & B_{66} \\ B_{11} & B_{12} & B_{16} & D_{11} & D_{12} & D_{16} \\ B_{12} & B_{22} & B_{26} & D_{12} & D_{22} & D_{26} \\ B_{16} & B_{26} & B_{66} & D_{16} & D_{26} & D_{66} \end{bmatrix} \begin{Bmatrix} \epsilon_{xx} \\ \epsilon_{\theta\theta} \\ \epsilon_{x\theta} \\ k_{xx} \\ k_{\theta\theta} \\ k_{x\theta} \end{Bmatrix} \tag{6}$$

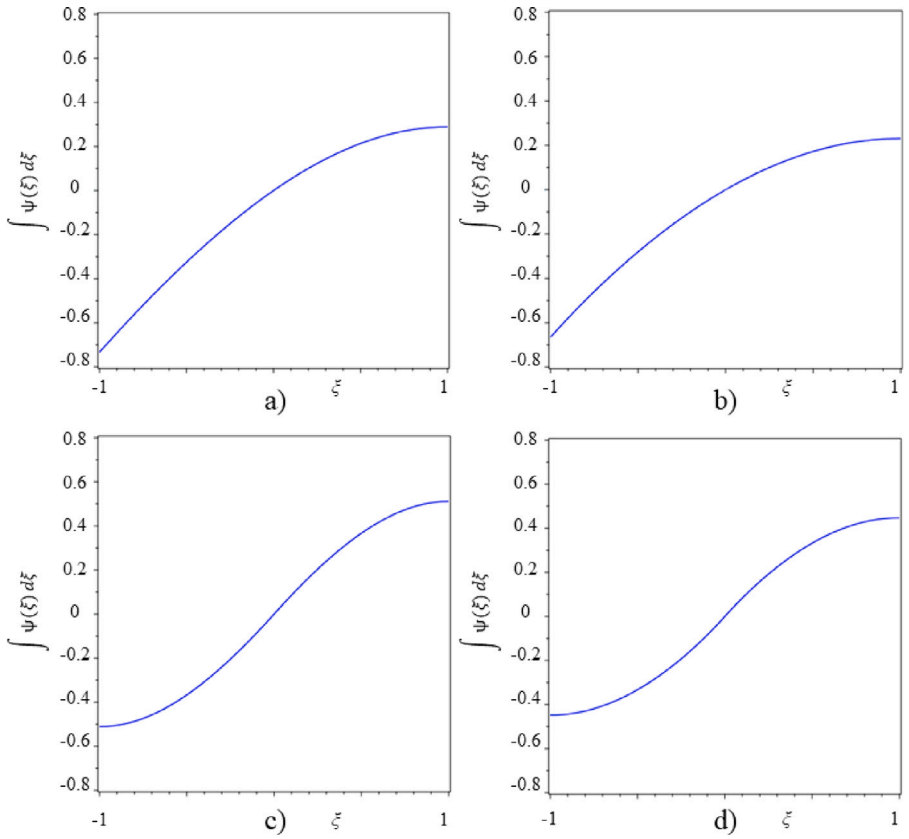

Fig. 2. Tow path representation for (a) linear variation of fibre orientation, (b) constant in-plane curvature, (c) linear variation of fibre orientation with two segments, (d) constant in-plane curvature with two segments ($T_0 = 70°$, $T_1 = 0°$).

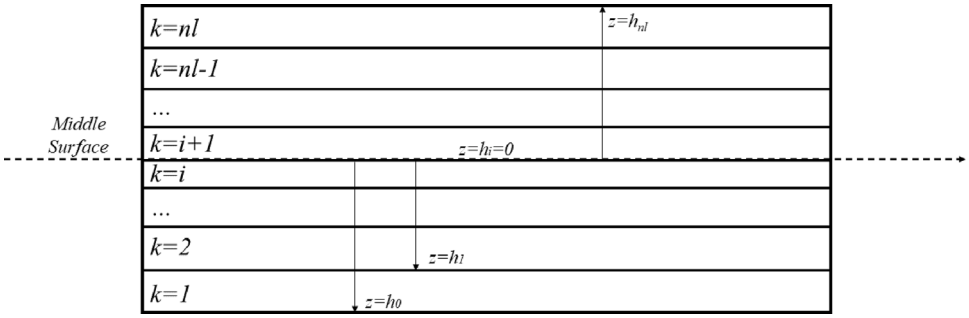

Fig. 3. Laminae stacking sequence and nomenclature.

The coefficients of the matrix are expressed in Eqs. (7), where $\overline{Q}_{ij}^{(k)}$ is a coefficient of the elastic matrix of the layer k on the cylindrical coordinate system. The index k refers to each layer in the order that is established by the stacking sequence represented in Fig. 3, where nl is the total number of layers of the shell.

$$A_{ij} = \sum_{k=1}^{nl} \overline{Q}_{ij}^{(k)} (h_k - h_{k-1}) \tag{7a}$$

$$B_{ij} = \frac{1}{2} \sum_{k=1}^{nl} \overline{Q}_{ij}^{(k)} (h_k^2 - h_{k-1}^2) \tag{7b}$$

$$D_{ij} = \frac{1}{3} \sum_{k=1}^{nl} \overline{Q}_{ij}^{(k)} (h_k^3 - h_{k-1}^3) \tag{7c}$$

To arrive at the coefficients of the elastic matrix on the cylindrical coordinate system, the transformation matrices shown in Eqs. (8) and (9) are used; they establish the relations between the stresses and strains in the material coordinate system and the cylindrical coordinate system, where $m = \cos(\psi)$ and $n = \sin(\psi)$. The material coordinate is referenced to with the indices 1, 2 and 3, that correspond to the direction parallel to the fibres, to its perpendicular in a plane tangent to the shell's surface and to the perpendicular to the shell's surface, respectively.

$$\begin{Bmatrix} \sigma_{xx} \\ \sigma_{\theta\theta} \\ \sigma_{zz} \\ \sigma_{\theta z} \\ \sigma_{xz} \\ \sigma_{x\theta} \end{Bmatrix} = \begin{bmatrix} m^2 & n^2 & 0 & 0 & 0 & -2\cdot m\cdot n \\ n^2 & m^2 & 0 & 0 & 0 & -2\cdot m\cdot n \\ 0 & 0 & 1 & 0 & 0 & 0 \\ 0 & 0 & 0 & m & n & 0 \\ 0 & 0 & 0 & -n & m & 0 \\ m\cdot n & -m\cdot n & 0 & 0 & 0 & m^2 - n^2 \end{bmatrix} \begin{Bmatrix} \sigma_1 \\ \sigma_2 \\ \sigma_3 \\ \sigma_{23} \\ \sigma_{13} \\ \sigma_{12} \end{Bmatrix} \tag{8}$$

$$\begin{Bmatrix} \epsilon_1 \\ \epsilon_2 \\ \epsilon_3 \\ \gamma_{23} \\ \gamma_{13} \\ \gamma_{12} \end{Bmatrix} = \begin{bmatrix} m^2 & n^2 & 0 & 0 & 0 & m\cdot n \\ n^2 & m^2 & 0 & 0 & 0 & -m\cdot n \\ 0 & 0 & 1 & 0 & 0 & 0 \\ 0 & 0 & 0 & m & -n & 0 \\ 0 & 0 & 0 & n & m & 0 \\ -2\cdot m\cdot n & 2\cdot m\cdot n & 0 & 0 & 0 & m^2 - n^2 \end{bmatrix} \begin{Bmatrix} \epsilon_{xx} \\ \epsilon_{\theta\theta} \\ \epsilon_{zz} \\ \gamma_{\theta z} \\ \gamma_{xz} \\ \gamma x\theta \end{Bmatrix} \tag{9}$$

Lastly, considering that the coefficients of the elastic matrix of the layer k on the material coordinate system Q_{ij}^{k} are given by Eq. (10), the expressions for $\overline{Q}_{ij}^{(k)}$ can be obtained, as seen in Eqs. (11), [1,54].

$$Q_{11} = \frac{E_{11}}{\Delta} \tag{10a}$$

$$Q_{22} = \frac{E_{22}}{\Delta} \tag{10b}$$

$$Q_{66} = G_{12} \tag{10c}$$

$$Q_{12} = E_{11}\frac{\nu_{21}}{\Delta} = E_{22}\frac{\nu_{12}}{\Delta} \tag{10d}$$

$$\Delta = 1 - \nu_{12}\nu_{21} \tag{10e}$$

$$\overline{Q}_{11} = Q_{11}m^4 + 2(Q_{12} + 2Q_{66})m^2n^2 + Q_{22}n^4 \tag{11a}$$

$$\overline{Q}_{12} = (Q_{11} + Q_{22} - 4Q_{66})m^2n^2 + Q_{12}(m^4 + n^4) \tag{11b}$$

$$\overline{Q}_{16} = (Q_{11} - Q_{12} - 2Q_{66})m^3n + (Q_{12} - Q_{22} + 2Q_{66})mn^3 \tag{11c}$$

$$\overline{Q}_{22} = Q_{11}n^4 + 2(Q_{12} + 2Q_{66})m^2n^2 + Q_{22}m^4 \tag{11d}$$

$$\overline{Q}_{26} = (Q_{11} - Q_{12} - 2Q_{66})mn^3 + (Q_{12} - Q_{22} + 2Q_{66})m^3n \tag{11e}$$

$$\overline{Q}_{66} = (Q_{11} - 2Q_{12} + Q_{22} - 2Q_{66})m^2n^2 + Q_{66}(m^4 + n4) \tag{11f}$$

Eqs. (6) and (7) are similar to the ones of traditional laminated composite shells [1]. However, in a variable stiffness cylindrical shell, coefficients A_{ij}, B_{ij} and D_{ij} change with the spatial coordinates, because so do m and n in Eq. (11). In this study, they are functions of the axial coordinate. Furthermore, the B_{ij} coefficients are null when there is lamination symmetry about the middle surface of the shell. This property is taken advantage of, since exploring the effects of asymmetry on a composite laminated shell is not the goal of this study. Also, note that for balanced layer setups, like $[\psi, -\psi]_s$, the terms A_{16} and A_{26} are null, and in the cases of cross ply laminates, where each laminate tow angle is either 0°or 90°, coefficients A_{16}, A_{26}, D_{16} and D_{26} are null. These relations are valid for variable stiffness as they are for constant stiffness composite laminated shells.

The equations of motion here used are the ones derived for thin cylindrical shells in [1], where Hamilton's principle was applied. Considering body forces p_i, in directions $i = x$, θ and z, these equations are

$$\frac{\partial N_{xx}}{\partial x} + \frac{1}{R}\frac{\partial N_{x\theta}}{\partial \theta} + p_x = \rho h\frac{\partial^2 u_0}{\partial t^2} \tag{12a}$$

$$\frac{1}{R}\frac{\partial N_{\theta\theta}}{\partial \theta} + \frac{\partial N_{x\theta}}{\partial x} + \frac{1}{R^2}\frac{\partial M_{\theta\theta}}{\partial \theta} + \frac{1}{R}\frac{\partial M_{x\theta}}{\partial x} + p_\theta = \rho h\frac{\partial^2 v_0}{\partial t^2} \tag{12b}$$

$$-\frac{N_{\theta\theta}}{R} + \frac{\partial^2 M_{xx}}{\partial x^2} + \frac{2}{R}\frac{\partial^2 M_{x\theta}}{\partial \theta \partial x} + \frac{1}{R^2}\frac{\partial^2 M_{\theta\theta}}{\partial \theta^2} + p_z = \rho h\frac{\partial^2 w_0}{\partial t^2} \tag{12c}$$

The cylindrical shell is submitted to an axial supersonic airflow on the outer surface, along the x axis, while the internal surface is submitted to the undisturbed atmospheric pressure. The resulting pressure is represented using the linear piston theory [2,55], with a curvature correction term [42,44,56,57]. This provides a relation between the surface's displacement and velocity and the aerodynamic pressure p_z, which renders a computationally inexpensive aerodynamic model. Hence, the aerodynamic pressure is given by

$$p_z = \underbrace{-\frac{\gamma p_\infty M^2}{\sqrt{M^2-1}}\cdot\left[\frac{\partial w}{\partial x} - \frac{1}{2R\sqrt{M^2-1}}\cdot w\right]}_{\text{Piston 1}} \underbrace{-\frac{\gamma p_\infty M^2}{\sqrt{M^2-1}}\cdot\frac{1}{Ma_\infty}\left(\frac{M^2-2}{M^2-1}\right)\cdot\frac{\partial w}{\partial t}}_{\text{Piston 2}} \tag{13}$$

Force components p_x and p_θ are considered to be null.

The aerodynamic pressure difference between the outer and internal surfaces at each point in space and time may be approximated by the linear equation (13) for $1.6 < M < 5$, [42,46]. This is a local, zero memory relation, since the pressure at a given position and time does not depend upon the motion at other positions and previous times [2]. This equation has terms that depend on the first time derivative of the displacements and terms that do not. It is convenient to distinguish them, so they will be designated as 'Piston 1' and 'Piston 2', respectively, as discriminated in the equation.

The ordinary differential equations representing the problem at hand are derived following a p-version finite element method [23] approach, here based on Galerkin's method. In this problem, where the geometry is simple and there are no discontinuities, the convergence rate of the p-version FEM is superior to the one of the h-version FEM; furthermore, although more than one element can naturally be used, a single element is enough, precluding the assembly stage [23,58–61]. The displacement vector $\mathbf{d}$ is as seen in Eq. (14), where $\mathbf{N}$ is the shape function matrix, Eq. (15), and the generalised coordinates $\mathbf{q_t}(t)$ are time-dependent functions.

$$\mathbf{d} = \begin{Bmatrix} u_0 \\ v_0 \\ w_0 \end{Bmatrix} = \mathbf{N}\cdot\mathbf{q_t}(t) \tag{14}$$

$$\mathbf{N} = \begin{bmatrix} \mathbf{ff_u} & \mathbf{0} & \mathbf{0} \\ \mathbf{0} & \mathbf{ff_v} & \mathbf{0} \\ \mathbf{0} & \mathbf{0} & \mathbf{ff_w} \end{bmatrix} \tag{15}$$

Vectors $\mathbf{ff_i}$, with $\mathbf{i} = \mathbf{u}, \mathbf{v}, \mathbf{w}$, are represented in Eqs. (16) and are the shape functions vectors for the u_0, v_0 and w_0 displacement components.

$$\mathbf{ff_u} = \{g_{u1}h_{u1}, g_{u1}h_{u2}, \ldots, g_{ui}h_{upt}, g_{u(i+1)}h_{u1}, g_{u(i+1)}h_{u2}, \ldots, g_{upm}h_{upt}\} \tag{16a}$$

$$\mathbf{ff_v} = \{g_{v1}h_{v1}, g_{v1}h_{v2}, \ldots, g_{vi}h_{vpt}, g_{v(i+1)}h_{v1}, g_{v(i+1)}h_{v2}, \ldots, g_{vpm}h_{vpt}\} \tag{16b}$$

$$\mathbf{ff_w} = \{f_1h_{w1}, f_1h_{w2}, \ldots, f_ih_{wpt}, f_{i+1}h_{w1}, f_{i+1}h_{w2}, \ldots, f_{po}h_{wpt}\} \tag{16c}$$

These bidimensional shape functions are obtained by the combination of unidimensional shape functions, out of three sets: the f set for the axial variation of the transversal displacement w_0, composed of the Hermite cubics for the first four functions, Eq. (17), and by the so-called Rodrigues form of Legendre polynomials for the other functions, Eq. (18) [58,62]; the g set for the axial variation of the membrane displacements u_0 and v_0, composed of the linear shape functions represented in Eq. (19) for the first two functions and by the set represented in Eq. (20) for the following [58,62]; and the h set for the angle variation of the displacements, composed of a subset of cosine functions for the u_0 and w_0 displacements and a subset of sine functions for the v_0 functions, Eqs. (21) [63–66].

$$f_1(\xi) = \frac{1}{2} - \frac{3}{4}\xi + \frac{1}{4}\xi^3 \tag{17a}$$

$$f_2(\xi) = \frac{1}{4} - \frac{1}{4}\xi - \frac{1}{4}\xi^2 + \frac{1}{4}\xi^3 \tag{17b}$$

$$f_3(\xi) = \frac{1}{2} + \frac{3}{4}\xi - \frac{1}{4}\xi^3 \tag{17c}$$

$$f_4(\xi) = -\frac{1}{4} - \frac{1}{4}\xi + \frac{1}{4}\xi^2 + \frac{1}{4}\xi^3 \tag{17d}$$

$$f_r(\xi) = \sum_{n=0}^{\mathrm{Int}(r/2)} \frac{(-1)^n(2r-2n-7)!!}{2^n n!(r-2n-1)!}\xi^{r-2n-1}\ ,\ r > 4 \tag{18}$$

$$g_1(\xi) = \frac{1}{2} - \frac{1}{2}\xi \tag{19a}$$

$$g_2(\xi) = \frac{1}{2} + \frac{1}{2}\xi \tag{19b}$$

$$g_r(\xi) = \sum_{n=0}^{\mathrm{Int}(r/2)} \frac{(-1)^n(2r-2n-5)!!}{2^n n!(r-2n-1)!}\xi^{r-2n-1}\ ,\ r > 2 \tag{20}$$

$$h_{ur}(\theta) = h_{wr}(\theta) = \cos(r\theta) \tag{21a}$$

$$h_{vr}(\theta) = \sin(r\theta) \tag{21b}$$

where $r!! = r(r-2)...(2 \text{ or } 1)$, $0!! = (-1)!! = 1$, and $\mathrm{Int}(r/2)$ denotes the integer part of $r/2$. Terms where negative values appear in (...)!! or in

the factorial are not calculated. The numbers of shape functions used from the h, g and f unidimensional sets are represented by p_t, p_m and p_o. The total number of degrees of freedom is $p_{tot} = (2 \cdot p_m + p_o) \cdot p_t$.

By considering or by disregarding the f_1, f_2, f_3, f_1, g_1 and g_2 functions, it is possible to account for the geometrical boundary conditions of the shell. These functions are also required to connect elements, although this is not relevant in this particular work, because a single p element is enough to represent the shell.

In this work, two type of boundary conditions were considered:

- both ends clamped

$$w_0 = v_0 = u_0 = \frac{\partial w_0}{\partial x} = 0, \text{ for } x = 0 \text{ and } x = l; \tag{22}$$

- both ends simply supported

$$w_0 = v_0 = M_x = N_x = 0, \text{ for } x = 0 \text{ and } x = l. \tag{23}$$

As said, Galerkin method is applied to derive the finite element matrices. For that purpose, the dynamic equilibrium equations (12) are multiplied by approximation functions. The resulting equations are integrated by parts in the domain; we only consider boundary conditions that allow to eliminate terms where evaluations at $\xi = 0$ and $\xi = l$ are performed. Due to continuity, all differences between terms evaluated at $\theta = 0$ and $\theta = 2\pi$ are null as well. Only after the integration by parts are internal forces and moments per unit length replaced, using the relations in Eq. (6). The ordinary differential equations of motion obtained in this way can be written as

$$\mathbf{M} \cdot \frac{\mathrm{d}^2}{\mathrm{d}t^2}\mathbf{q_t}(t) + \mathbf{K} \cdot \mathbf{q_t}(t) = \mathbf{p}(t) \tag{24}$$

where $\mathbf{M}$ represents the mass matrix, $\mathbf{K}$ the structural stiffness matrix and vector $\mathbf{p}$ contains the generalised forces due to fluid–structure interaction. The diverse terms that constitute matrices $\mathbf{M}$ and $\mathbf{K}$ can be found in Appendix A.

When there is no interaction with air, vector $\mathbf{p}(t)$ - Eq. (24) - is null. To find the modes of vibration in this conservative problem, one can assume that $\mathbf{q_t}(t) = \mathbf{q} \cdot \cos(\omega \cdot t)$ which results in Eq. (25) that defines a generalised eigenvalue problem.

$$\mathbf{K} \cdot \mathbf{q} = \omega^2 \cdot \mathbf{M} \cdot \mathbf{q}, \tag{25}$$

The eigenvalues, ω_i^2, with i taking values from 1 to p_{tot}, correspond to the squared natural frequencies of vibration; each eigenvector $\mathbf{q}_i$ multiplied by the shape function matrix defines the correspondent natural mode shape. Therefore, the motion under free vibration of a given natural mode is equal to $\mathbf{N} \cdot \mathbf{q}_i \cdot \cos(\omega_i \cdot t)$.

Including the terms of Eq. (13), when Galerkin's Method is applied to Eqs. (12), the ordinary differential equations of motion can be written in the following form

$$\mathbf{M} \cdot \frac{\mathrm{d}^2}{\mathrm{d}t^2}\mathbf{q_t}(t) + \mathbf{F_{Piston\,2}} \cdot \frac{\mathrm{d}}{\mathrm{d}t}\mathbf{q_t}(t) + \left(\mathbf{K} + \mathbf{F_{Piston\,1}}\right) \cdot \mathbf{q_t}(t) = 0 \tag{26}$$

Matrices $\mathbf{F_{Piston\,1}}$ and $\mathbf{F_{Piston\,2}}$ are explicitly given in Appendix B. It is noticeable that $\mathbf{F_{Piston\,1}}$ affects the system's stiffness and $\mathbf{F_{Piston\,2}}$ appears as a viscous damping term (physically, though, this term can introduce energy in the system, instead of damping the oscillations).

By introducing the vector of state space coordinates, composed of sub-vectors $\mathbf{y_t} = \frac{\mathrm{d}}{\mathrm{d}t}\mathbf{q_t}(t)$ and $\mathbf{q_t}(t)$ that represent the velocity and displacement fields, respectively, Eq. (26) is rearranged into Eq. (27).

$$\begin{bmatrix} \mathbf{M} & \mathbf{0} \\ \mathbf{0} & -\mathbf{M} \end{bmatrix} \begin{Bmatrix} \frac{\mathrm{d}}{\mathrm{d}t}\mathbf{y_t}(t) \\ \frac{\mathrm{d}}{\mathrm{d}t}\mathbf{q_t}(t) \end{Bmatrix} + \begin{bmatrix} \mathbf{F_{Piston\,2}} & \mathbf{K} + \mathbf{F_{Piston\,1}} \\ \mathbf{M} & \mathbf{0} \end{bmatrix} \begin{Bmatrix} \mathbf{y_t}(t) \\ \mathbf{q_t}(t) \end{Bmatrix} = \begin{Bmatrix} \mathbf{0} \\ \mathbf{0} \end{Bmatrix} \tag{27}$$

By assuming that

$$\begin{Bmatrix} \mathbf{y_t}(t) \\ \mathbf{q_t}(t) \end{Bmatrix} = \begin{Bmatrix} \mathbf{y} \\ \mathbf{q} \end{Bmatrix} \cdot e^{\Omega \cdot t} \tag{28}$$

the generalised eigenvalue problem seen in Eq. (29) is obtained

$$\Omega \begin{bmatrix} -\mathbf{M} & \mathbf{0} \\ \mathbf{0} & \mathbf{M} \end{bmatrix} \begin{Bmatrix} \mathbf{y} \\ \mathbf{q} \end{Bmatrix} = \begin{bmatrix} \mathbf{F_{Piston\,2}} & \mathbf{K} + \mathbf{F_{Piston\,1}} \\ \mathbf{M} & \mathbf{0} \end{bmatrix} \begin{Bmatrix} \mathbf{y} \\ \mathbf{q} \end{Bmatrix} \tag{29}$$

Table 1
Convergence study of the lowest natural frequency ω_1 for a three layered, cross-ply [0°/90°/0°] circular cylindrical shell with C-C boundary conditions ($R = 1$ m, $l/R = 5$, $h/R = 0.002$, $E_{22} = 7.6$ GPa, $E_{11}/E_{22} = 2.5$, $G_{12} = 4.1$ GPa, $\upsilon_{12} = 0.26$, $\rho = 1643$ kg/m^3).

p_m	p_o	p_t	p_{tot}	ω_1 [Hz]	*DIF %*
4	4	4	48	34.8120	170.9
7	7	7	147	13.0928	1.841
10	10	10	300	12.8672	0.086
13	13	13	507	12.8583	0.017
16	16	16	768	12.8561	0
4	14	14	308	12.8661	0.078
7	14	14	392	12.8600	0.030
10	14	14	476	12.8593	0.025
14	4	14	448	12.8914	0.275
14	7	14	490	12.8701	0.109
14	10	14	532	12.8643	0.064
14	14	4	168	22.0536	71.54
14	14	7	294	12.8584	0.018
14	14	10	420	12.8584	0.018
14	14	14	588	12.8583	0.017

Eigenvalues Ω are complex conjugate pairs that contain a real component $\Re\mathrm{e}(\Omega)$ and an imaginary part $\Im\mathrm{m}(\Omega)$. The eigenvectors are also complex conjugate pairs. It may be worth noting that by adding the complex conjugates, the dynamic response only presents a real component. Nonetheless, in the numerical tests we will only look at one of the terms (hence complex, in general). The real part of the eigenvalues affects the damping of the system and the dynamic response tends to a stable equilibrium solution if this value is negative. The imaginary part represents the frequency of the oscillating movement. Flutter occurs for flow conditions where the real component of at least one eigenvalue Ω changes to a positive value and the imaginary component – the frequency – is not null. If the change in the real component coincides with a null imaginary part (frequency), the structure became statically unstable; this phenomenon is called divergence [2].

3. Convergence and verification

As standard when FEM models are implemented, convergence tests were carried out with the intention of determining the number of degrees of freedom required for the results to converge to a solution. In the present specific model, it is also interesting to analyse the number of degrees of freedom related to the diverse displacement components and, within each of these, the importance of axial and radial functions.

The results of one of the convergence tests performed are presented in Table 1. This regards the computation of the fundamental natural frequency of composite laminated cylindrical shell clamped at both ends. It is recalled that p_m, p_o, p_t and p_{tot} are the number of shape functions used from the g, f and h sets and the total number of degrees of freedom, respectively, and that sets g and f are functions of ξ, whilst set t contains functions of θ. The relative differences with respect to the solution computed with $p_m = p_o = p_t = 16$ are given in column DIF %.

The table is divided in four sections, with the last three focusing on convergence with the variation of the number of functions of a single type. It is verified that four membrane shape functions and four transverse shape functions for the longitudinal direction lead to accurate results. More radial shape functions (the functions of θ, number p_t) are needed for convergence, because the respective mode shape of vibration (not shown) has several waves in the circumferential direction. If we wish to study only this mode, loosing the generality of the FEM model, the number of degrees of freedom can be reduced by choosing only the necessary functions of θ.

Values obtained for the free vibration of circular cylindrical shells by the model described in this document are compared with values found in the literature in Tables 2 and 3, which present a comparison of the adimensional frequency parameter $\Omega = \omega R\sqrt{\rho/E_{22}}$ for two

Table 2
Frequency parameters $\Omega = \omega R\sqrt{\rho/E_{22}}$ for a three layered, cross-ply [0°/90°/0°] circular cylindrical shell with C-C and S-S boundary conditions ($l/R = 5$, $h/R = 0.002$, $E_{22} = 7.6$ GPa, $E_{11}/E_{22} = 2.5$, $G_{12} = 4.1$ GPa, $\upsilon_{12} = 0.26$, $\rho = 1643$ kg/m^3, $m = 1$).

n	C-C boundary conditions			S-S boundary conditions			
	Present work	Ref. [66]	Ref. [67]	Present work	Ref. [66]	Ref. [68]	Ref. [69]
1	0.303168	0.303318	0.303609	0.248635	0.248637	0.248635	0.248634
2	0.166909	0.167166	0.167527	0.107203	0.107206	0.107203	0.107202
3	0.099194	0.099440	0.099667	0.055087	0.055090	0.055087	0.055085
4	0.064400	0.064607	0.064699	0.033790	0.033793	0.033790	0.033788
5	0.046171	0.046322	0.046345	0.025794	0.025796	0.025794	0.025790
6	0.038128	0.038233	0.038222	0.025877	0.025878	0.025877	0.025873

Table 3
Frequency parameters $\Omega = \omega R\sqrt{\rho/E_{22}}$ of the fundamental natural frequency for a four layered, angle-ply circular cylindrical shell with C-C and S-S boundary conditions ($l/R = 4$, $h/R = 0.01$, $E_{11}/E_{22} = 20$, $G_{12}/E_{22} = 0.65$, $\upsilon_{12} = 0.25$).

Lamination	C-C boundary conditions			S-S boundary conditions		
	Present work	Ref. [70]	Ref. [71]	Present work	Ref. [70]	Ref. [71]
$[+30°/-30°]_s$	0.1827	0.1818	0.1827	0.1237	0.1233	0.1232
$[+45°/-45°]_s$	0.1768	0.1760	0.1789	0.1196	0.1195	0.1193
$[+60°/-60°]_s$	0.1801	0.1780	0.1796	0.1097	0.1094	0.1093

Table 4
Critical free stream pressure p_{crit} for the occurrence of flutter for S-S boundary conditions of circular cylindrical shells with the following parameters: $G_{12} = E_{11}/[2 \cdot (1+\upsilon_{12})]$, $h = 0.0001015$ m, $R = 0.203$ m, $\rho = 8900$ kg/m^3, $M = 3$, $a_\infty = 213$ m/s, $\gamma = 1.4$, $l = 0.381$ m, $\upsilon_{12} = 0.35$, $E_{11} = E_{22} = 110 \cdot 10^9$ GPa, $pm = po = 10$, $pt = 30$.

Reference	p_{crit} [Pa]	n_{crit}
Present work	3864	25
FEM Ref. [41]	3875	26
FEM Ref. [43]	3599	26
Analytical Ref. [72]	3792	25

Table 5
Critical free stream pressure p_{crit} for the occurrence of flutter for S-S boundary conditions of circular cylindrical shells with the following parameters: $G_{12} = E_{11}/[2 \cdot (1+\upsilon_{12})]$, $h = 0.0001015$ m, $R = 0.203$ m, $\rho = 8900$ kg/m^3, $M = 3$, $a_\infty = 213$ m/s, $\gamma = 1.4$, $l = 0.406$ m, $\upsilon_{12} = 0.33$, $E_{11} = E_{22} = 89 \cdot 10^9$ GPa, $pm = po = 10$, $pt = 30$.

Reference	p_{crit} [Pa]	n_{crit}
Present work	2757	25
Analytical Ref. [39]	2896	24
FEM Ref. [43]	2633	25

different cases of constant stiffness shells; m corresponds to the number of axial waves of a given natural mode shape, and n corresponds to the number of circumferential waves. The results are very close to those found in the literature.

To close this section, a comparison of the critical values of free stream static pressure, p_{crit}, that result in the occurrence of aerodynamic flutter is made. Results are presented in Tables 4 and 5.

The values of the critical free stream pressure computed by the different authors differ more than in the natural frequencies case. However, the critical stream pressure values of the present approach are still reasonably close to those found by other authors, with the absolute value of the relative difference ranging from 0.2% to 7%. A difference between the number of waves of the critical flutter mode shape is also observed. This difference may come from the fact that the corresponding p_{crit} is sometimes close to the values of p_{crit} of modes with a different number of circumferential waves and a slight difference in the mathematical/numerical model may result in different modes achieving flutter first. It is also found that the critical flutter modes may correspond to mode shapes with a high number of circumferential waves and, therefore, this should be considered when choosing the number of shape functions used from the h set.

Table 6
Shell and airflow parameters for the performed tests.

Young's modulus E_{11}	126.3 GPa
Young's modulus E_{22}	8.765 GPa
Shear modulus G_{12}	4.92 GPa
Poisson's ratio υ_{12}	0.334
Shell's volumetric mass ρ	1557 kg/m^3
Shell's thickness h	0.0001015 m
Shell's axial length l	0.406 m
Shell's radius R	0.203 m
Mach M	3.5
Air's adiabatic exponent γ	1.4
Air's speed of sound a_∞	213 m/s

4. Supersonic flutter of fibre reinforced composite laminated cylindrical shells

In this section, various fibre paths are tested with the objective of finding curvilinear paths that enable an increase of the critical free stream static pressure p_{crit} associated with aeroelastic instabilities. Unless stated otherwise, it is considered that the circular cylindrical composite shell and the airflow have the properties stated in Table 6. These parameters were chosen to be similar to those found in Refs. [32,37,43,72]. There is no viscous or structural damping and the shell is composed of 12 layers $[\pm\psi]_s$ with a balanced and symmetric setup, where the tow angle ψ might be constant or a function of the axial coordinate. No manufacturing defects and material imperfections are considered. More fibre paths than those found in this section were tested, the results shown are a selection.

4.1. Shells with clamped boundary conditions

First, numerical tests were performed in order to find lamination parameters that increase the value of p_{crit}. C-C boundary conditions are considered. Five fibre paths were tested: constant angle, linear variation of fibre orientation (with 1 and 2 segments) and constant in-plane curvature (with 1 and 2 segments). The last four are represented in Fig. 2.

Fibre paths must have a turning radius r_ψ that respects a minimum value. This is important to avoid defects promoted by in-plane bending deformations, such as local buckling and wrinkling of the inner edges of the fibres, which can cause a decline in mechanical properties. Therefore, in the performed tests, a minimum turning radius of 635 mm is considered (which is a typical value for the minimum turning radius of a 32 tow course with 3.175 mm wide tows [11]). In addition to that,

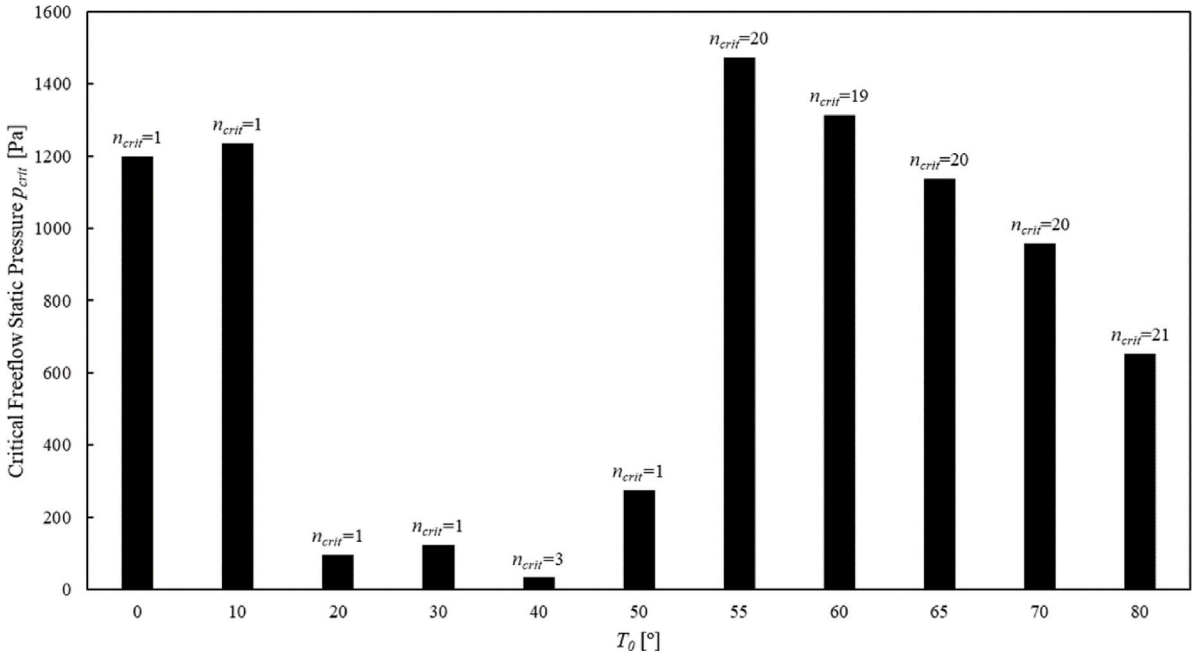

Fig. 4. p_{crit} and n_{crit} for various values of T_0 of a CSCL cylindrical shell.

to avoid problematic scenarios in manufacturing, the tow angle ψ at any point of the structure respects the condition $\psi \in [0°, 85°]$.

Also, as seen in the model validation, flutter occurs for mode shapes with high numbers of circumferential waves, and, therefore, tests are performed with a number of shape functions that allow up to $n = 25$ circumferential waves. For the T_0 and T_1 parameters of each type of fibre path that resulted in the highest value of p_{crit}, an additional test was performed with a number of shape functions that allowed up to $n = 40$ circumferential waves, to further validate the results. Furthermore, the number of shape functions used from the g and f set are, respectively, $p_m = 8$ and $p_o = 8$. These parameters were chosen to achieve an acceptable balance between processing time and result accuracy. Naturally, mode shapes with an extremely high number of circumferential (more than 25) and axial waves are not reliably represented, except for the previously mentioned cases where higher values of n were employed in order to verify the results accuracy.

Lastly, to calculate the critical free stream pressure p_{crit} at which flutter occurs, plots are developed where the eigenvalues Ω of generalised eigenvalue problem (29) are calculated for various values of p_∞. The eigenvalue problem is solved for values of p_∞ with a resolution of 20 Pa. Therefore, calculations are made for $p_\infty \in \{0, 20, 40, 60, 80, 100, \ldots\}$ [Pa]. Then, a linear interpolation is made between the calculated values to find Ω for any p_∞.

An iterative process, where fibre path parameters T_0 and T_1 are progressively tweaked, is adopted to find fibre paths that increase the value of p_{crit}. Since not all possibilities are explored, the highest value found for p_{crit} is not necessarily the highest possible. By applying an optimisation process [3], further improvements may eventually be achieved. Nonetheless, higher values of p_{crit} are obtained using curvilinear instead of straight fibres.

4.1.1. Constant stiffness composite laminates

Firstly, the tow angle of a straight fibre that enables the biggest increase of p_{crit} was searched for. For these paths, the only parameter that exists is T_0. Various values of T_0 were tested, by sequential increments of 10°, and then, around high values of p_{crit}, T_0 was varied by 5°. The results obtained can be seen in Fig. 4.

A maximum value of $p_{crit} = 1474$ Pa was obtained for $T_0 = 55°$. The corresponding shapes – real part, imaginary part and absolute value – are represented in Fig. 5; the number of circumferential waves is $n_{crit} = 20$. On the other hand, the minimum value of pressure obtained is $p_{crit} = 32$ Pa for $T_0 = 40°$, corresponding to a shape with a number of circumferential waves equal to $n_{crit} = 3$. This shape can be seen in Fig. 6. In the figure captions, designation "flutter mode shape" is employed to designate shapes assumed by the shell when flutter arises; this designation will be often applied in the article.

It is noticeable that a small change in tow angle can originate a significant difference in p_{crit}. Additionally, it is seen that for different values of T_0, flutter can be achieved by modes with different numbers of circumferential and axial waves, hence with different shapes. The variation of the critical flutter pressure with T_0 will be explained in a sub-section below, where the modes of vibration of modes that couple in flutter are addressed.

When dealing with curvilinear fibre paths, the value of $p_{crit} = 1474$ Pa is used as a benchmark, with the goal of finding tow paths that surpass this value.

4.1.2. VSCL with linear angle variation paths: 1 segment

The linear angle variation type fibre path, with one segment, is analysed in this section. The starting parameters for the iteration process were $\langle 55°, 55° \rangle$, which correspond to the constant angle fibre path that led to the highest critical pressure in the former section. From there, parameter tweaks were progressively made in search for an increase of the value of p_{crit}. The results of the tests performed are presented in Table 7, along with the minimum turning radius r_ψ of each path.

It is seen in Table 7 that the values of p_{crit} can be significantly increased by using curvilinear fibres. The highest value with an admissible curvature radius is highlighted and corresponds to the $\langle 40°, 80° \rangle$ fibre path. Comparing the maximum values of p_{crit} obtained with the straight fibre path, 1474 Pa, and with this curvilinear fibre path, 2368 Pa, a relative increase of 60.7% is observed. The flutter mode shape corresponding to the $\langle 40°, 80° \rangle$ fibre path is plotted in Fig. 7. This shape contains $n_{crit} = 16$ circumferential waves.

As a verification test, the values of p_{crit} for $\langle 60°, 50° \rangle$ and $\langle 50°, 60° \rangle$ were calculated and the same result, $p_{crit} = 1697$ Pa, was obtained. This is as expected, since the paths are similar, but symmetric with respect to a longitudinal line. Additionally, Table 7 contains paths deemed to be invalid, for not respecting the minimum turning radius manufacturing constraint. From these paths, the highest value obtained is $p_{crit} = 3287$ Pa, which further shows the potential of the variable

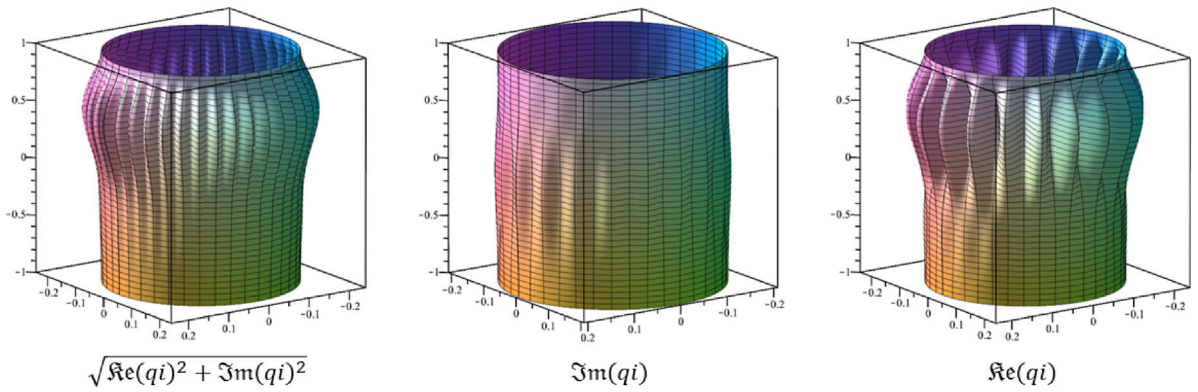

Fig. 5. Critical flutter mode shape of a CSCL shell with $T_0 = 55°$ ($n_{crit} = 20$).

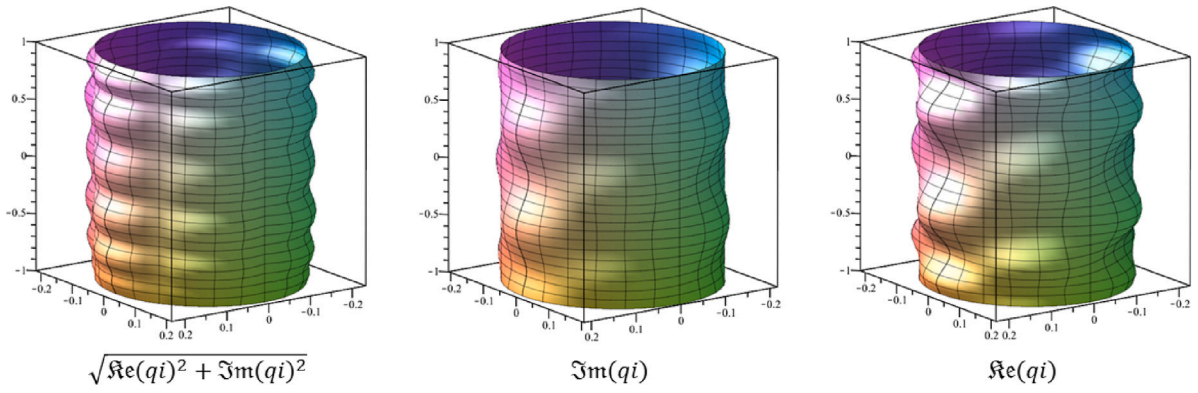

Fig. 6. Critical flutter mode shape of a CSCL shell with $T_0 = 40°$ ($n_{crit} = 3$).

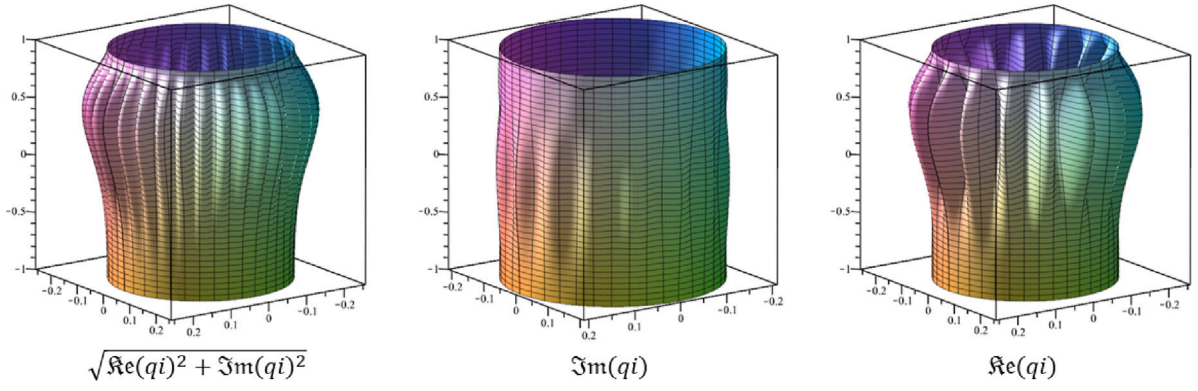

Fig. 7. Critical flutter mode shape of a VSCL shell with a $\langle 40°, 80° \rangle$ fibre path ($n_{crit} = 16$).

stiffness concept for the improvement of the critical flutter speed, even if, with the manufacturing constraints here accepted, the fibre path corresponding to the latter value is not achievable. A justification for the improvements in p_{crit} is provided in Section 4.1.6 of this paper.

4.1.3. VSCL with constant in-plane curvature paths: 1 segment

Now, constant in-plane curvature fibre paths, still one segment, are examined. The path parameters corresponding to the highest value of p_{crit} obtained for a linear angle variation fibre path, one segment, was used as a starting point for the iterative procedure. The results obtained in these tests are given in Table 8.

The value of p_{crit} for a $\langle 40°, 80° \rangle_c$ tow path is equal to 2149 Pa. This value is lower than the one corresponding to a shell with the linear angle variation path $\langle 40°, 80° \rangle$, which is equal to p_{crit} = 2368 Pa. Naturally, even though parameters T_0 and T_1 have the same value, the two paths differ, in this case leading to a worse performance of the constant in-plane curvature fibre path, one segment. The relative difference in the value of p_{crit} is −8.8%.

However, Table 8 reveals that higher values of p_{crit} were found for the constant in-plane curvature tow paths than for the linear angle variation paths, both with one segment. One reason for this is the fact that a bigger difference between T_0 and T_1 can be achieved using the constant in-plane curvature tow path, since the manufacturing constraint restricts less severely this type of path. Therefore, for the same minimum turning radius allowed, there is more freedom on the parameters choices.

The highest value of critical free stream pressure obtained, p_{crit} = 3164 Pa, is highlighted; it corresponds to the $\langle 25°, 85° \rangle_c$ path. This value of p_{crit} corresponds to an increase of 114.7% in relation to the highest value obtained for a constant angle path. The flutter mode shape is

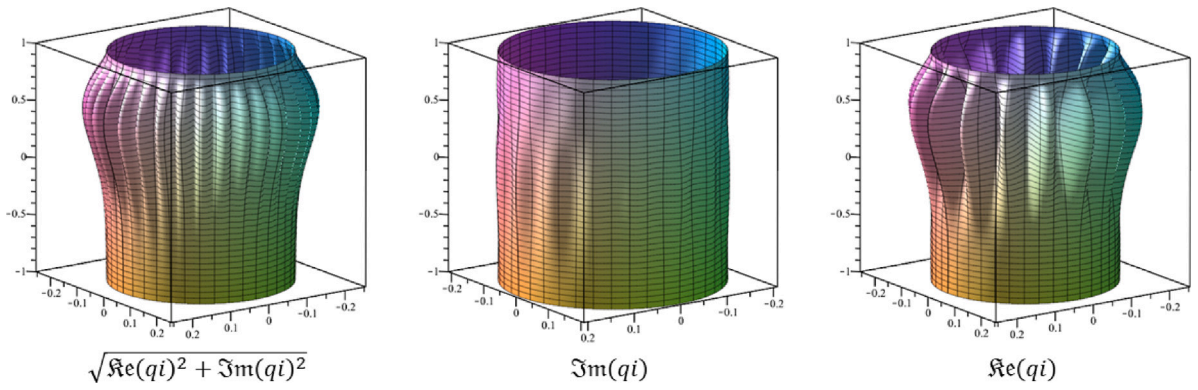

Fig. 8. Critical flutter mode shape of a VSCL shell with a $\langle 25°, 85° \rangle_c$ fibre path ($n_{crit} = 16$).

Table 7
Critical free stream pressure p_{crit} for shells with linear angle variation fibre paths $\langle T_0, T_1 \rangle$.

T_0 [°]	T_1 [°]	r_ψ [m]	p_{crit} [Pa]
55	55	–	1474
60	50	3.6189	1697
50	60	3.6189	1697
50	80	1.2063	1922
40	80	0.7592	**2368**
40	75	0.8676	2328
40	85	0.6748	2280
Inadmissible Paths ($r_\psi < 635$ mm):			
T_0 [°]	T_1 [°]	r_ψ [m]	p_{crit} [Pa]
30	80	0.5372	2805
20	80	0.4126	3237

Table 8
Critical free stream pressure p_{crit} for shells with constant in-plane curvature paths $\langle T_0, T_1 \rangle_c$.

T_0 [°]	T_1 [°]	r_ψ [m]	p_{crit} [Pa]
40	80	1.1871	2149
30	85	0.8182	2909
25	85	0.7078	**3164**
25	80	0.7222	3134

Table 9
Critical free stream pressure p_{crit} for shells with linear angle variation fibre paths $\langle T_1, T_0, T_1 \rangle$.

T_0 [°]	T_1 [°]	r_ψ [m]	p_{crit} [Pa]
30	50	0.6715	323
55	80	0.8111	1803
55	85	0.6759	**1816**
60	85	0.9305	1659
Inadmissible Paths ($r_\psi < 635$ mm):			
T_0 [°]	T_1 [°]	r_ψ [m]	p_{crit} [Pa]
80	30	0.2686	119
30	80	0.2686	2896

graphically represented in Fig. 8, which corresponds to a mode shape with $n_{crit} = 16$ circumferential waves, similarly to the one obtained in the $\langle 40°, 80° \rangle$ tow path.

4.1.4. VSCL with linear angle variation paths: 2 segments

The design flexibility of VSCL shells can be further improved by dividing the fibre path into different sections, each with its own shape and T_0 and T_1 parameters, as long as the continuity of the fibre is ensured. This concept is now tested with paths with two anti-symmetric segments.

Firstly, tests were performed for fibre paths with two segments with linear angle variation $\langle T_1, T_0, T_1 \rangle$, whose results are seen in Table 9. Higher values of p_{crit} were achieved with the linear angle variation fibre paths with 1 segment. This is due to that fact that, while the fibre path allows to create more complex paths, the minimum turning radius manufacturing constraint further restricts the difference that the parameters T_0 and T_1 can have between them, which may not be beneficial to the structure's mechanical properties. For instance, for the parameters of $T_0 = 30°$and $T_1 = 80°$, the fibre path with 1 segment has a minimum turning radius of $r_\psi = 537.2$ mm, while the path with 2 segments has a minimum turning radius of $r_\psi = 268.6$ mm, which is considerably lower. Table 9 contains inadmissible paths, due to their turning radius, that further illustrate this point. A value of $p_{crit} = 2896$ Pa was obtained for the path $\langle 80°, 30°, 80° \rangle$, which is a higher result than those found for the paths with 1 segment. Unfortunately, as it was stated, manufacturing shells with this fibre path would likely result out-of-plane tow buckling, that would harm the mechanical performance of the structure. Analysing the inadmissible paths, it is seen that different values of p_{crit} are obtained by swapping the values between T_0 and T_1, as it would be expected. In contrast with the fibre paths with 1 segment, fibre paths with 2 segments with swapped T_0 and T_1 parameters are not symmetric versions of each other and, therefore, the obtained value of p_{crit} should not be the same.

Regarding the admissible paths, the biggest value of p_{crit} was obtained for the $\langle 85°, 55°, 85° \rangle$ fibre path, which is highlighted and corresponds to $p_{crit} = 1816$ Pa. This is equal to a relative increase of 23.2% regarding the highest obtained value of p_{crit} for the constant angle paths. The corresponding flutter mode shape is graphically represented in Fig. 9, and it has $n_{crit} = 16$ circumferential waves.

4.1.5. VSCL with constant in-plane curvature paths: 2 segments

Similarly to the previously tested fibre path, the constant in-plane curvature path can also be divided into 2 segments. The results obtained are presented in Table 10, where the pattern observed in previous tests repeats itself. Comparing the constant in-plane curvature path with 1 and 2 segments, the one with 1 segment tends to yield higher values, due to the fact that the manufacturing constraint of the minimum turning radius, in the case of the path with 2 segments, restricts more severely the values that the T_0 and T_1 parameters can have. It is noticed that, in these cases, a bigger difference between the T_0 and T_1 parameters tends to increase the value of p_{crit}.

The values of p_{crit} of the $\langle 85°, 55°, 85° \rangle_c$ fibre path and the $\langle 85°, 55°, 85° \rangle$ path were calculated and compared. For the constant curvature one, the value of $p_{crit} = 1779$ Pa was obtained, which corresponds to a relative difference of −2.0% in relation to the one obtained for the linear angle variation path with 2 segments.

Even though the obtained value for the same parameters of T_0 and T_1 is lower for the constant in-plane curvature path than for the linear angle variation path (both with 2 segments), this type of path has a

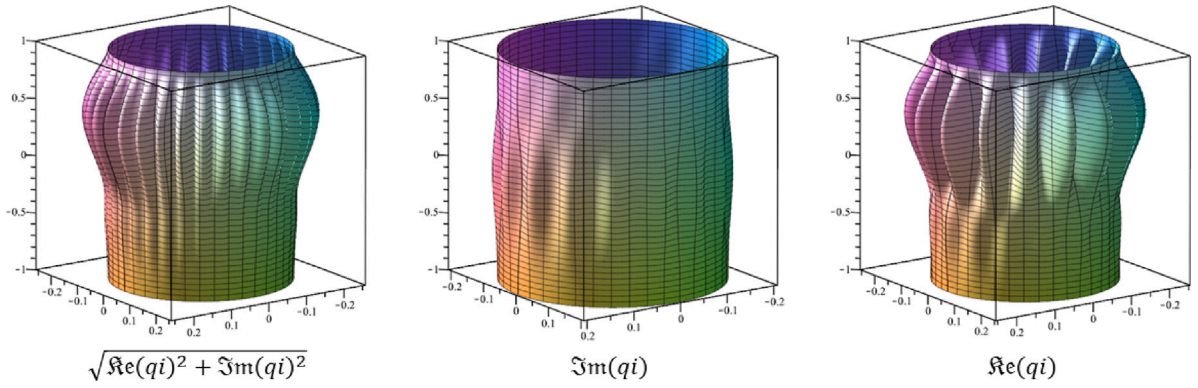

Fig. 9. Critical flutter mode shape of a VSCL shell with a $\langle 85°, 55°, 85° \rangle$ fibre path ($n_{crit} = 16$).

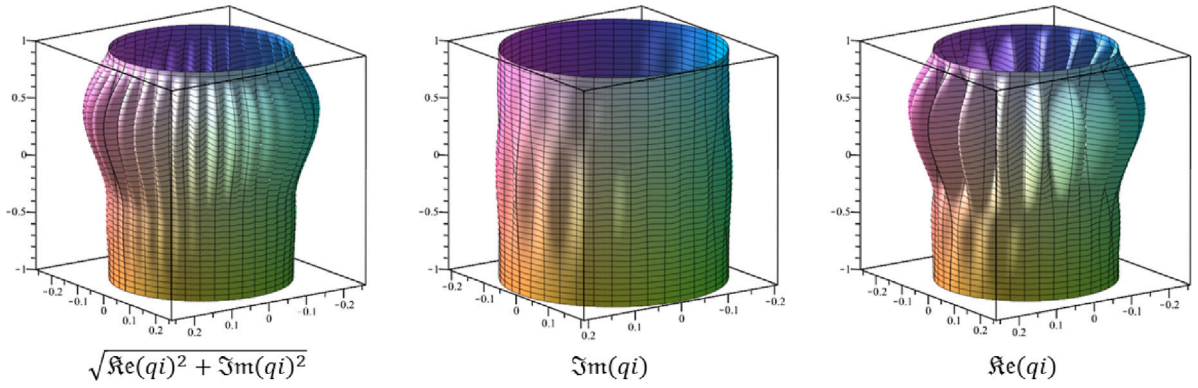

Fig. 10. Critical flutter mode shape of a VSCL shell with a $\langle 85°, 45°, 85° \rangle_c$ fibre path ($n_{crit} = 17$).

Table 10
Critical free stream pressure p_{crit} for shells with constant in-plane curvature fibre paths $\langle T_1, T_0, T_1 \rangle_c$.

T_0 [°]	T_1 [°]	r_ψ [m]	p_{crit} [Pa]
55	85	1.1466	1779
45	85	0.7022	**2146**
45	80	0.7310	2136
50	85	0.8820	1953

bigger flexibility in the definition of T_0 and T_1, which allowed achieving better results overall. The biggest value of p_{crit} obtained for this type of path is highlighted in Table 10 and is equal to 2146 Pa. This value corresponds to the $\langle 85°, 45°, 85° \rangle_c$ path, and its critical flutter mode shape has $n_{crit} = 17$ circumferential waves as represented in Fig. 10.

4.1.6. Frequency analysis

In the tests performed on clamped shells, a significant increase of the value of p_{crit} was achieved by using curvilinear fibres. In this section, the relation between the increase of p_{crit} and the imaginary part of the eigenvalues $\Im m(\Omega)$ is analysed.

The highest obtained value of p_{crit} for a constant angle fibre path is $p_{crit} = 1474$ Pa and corresponds to the $\psi = 55°$path. In all tests performed with curvilinear fibres, the $\langle 25°, 85° \rangle_c$ fibre path was the one that led to the highest value of p_{crit}, specifically $p_{crit} = 3164$ Pa, which represents a relative increase of 114.7% in relation to the highest value obtained for a constant stiffness shell. These two fibre paths are chosen for the comparison of oscillation frequencies.

Fig. 11 contains the $\Re e(\Omega)$ and $\Im m(\Omega)$ plots along p_∞ of the critical flutter mode and its corresponding coupled mode of the shells with these two paths. In the $\Im m(\Omega)$ plot, the evolution of the frequency of the modes with p_∞ can be analysed. As expected, the frequencies of the modes start at different values and, at a higher value of p_∞, they converge. For $p_\infty = 0$ Pa, null aerodynamic pressure, the value of $\Im m(\Omega)$ corresponds to the value of the natural frequencies of the shell without fluid–structure interaction.

The natural frequencies of these modes are equal to 1844 rad/s and 1961 rad/s for the CSCL shell, and they are equal to 1052 rad/s and 1522 rad/s on the VSCL shell; hence, the difference between the two values is significantly higher for the VSCL shell. This higher difference results in higher values of p_{crit}, since, in the $\Im m(\Omega)$ plot, the values start further apart and, therefore, require a higher value of p_∞ to converge. The natural mode shapes of vibration, without aerodynamic effects, of all these cases are represented in Fig. 12.

The natural frequencies and mode shapes of vibration of the modes involved in flutter are strongly affected by the fibre paths. Therefore, the latter can be adjusted to increase the difference between of the natural frequencies of vibration of those modes, leading to an increase of the critical flutter pressure.

4.2. Simply supported boundary conditions comparison

In the previous section, it was demonstrated that curvilinear fibre paths can be used to achieve larger critical flutter pressures in cylindrical shells with clamped edges. In this section, the highest values of p_{crit} obtained for each type of fibre path with clamped edges are compared to the same paths, with the same parameters and number of shape functions used, but with simply supported edges. The goal is to investigate how the boundary conditions affect the values of p_{crit} and associated flutter mode shapes. The results obtained can be seen in Table 11.

It is generally seen that the values of p_{crit}, for the same fibre path, tend to decrease in shells with simply supported edges. Figs. 13–17 contain the graphical representation of the critical flutter mode shapes of the shells with S-S boundary conditions and with the $\psi = 55°$,

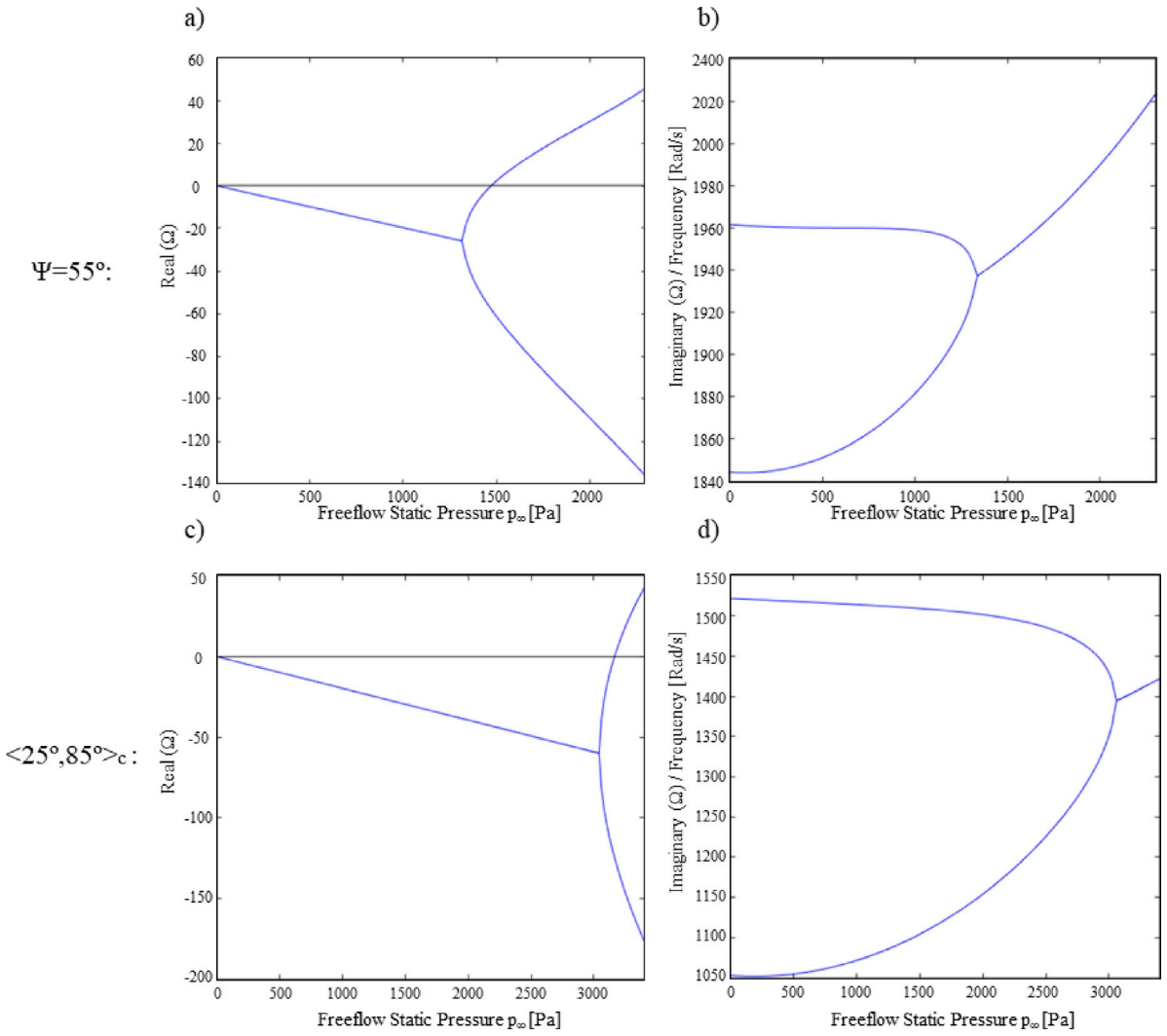

Fig. 11. Ω versus p_{∞}, critical flutter mode and corresponding coupled mode: (a) $\Re\mathfrak{e}(\Omega)$, constant stiffness shell with $\psi = 55°$; (b) $\Im\mathfrak{m}(\Omega)$, constant stiffness shell with $\psi = 55°$; (c) $\Re\mathfrak{e}(\Omega)$, shell with a $\langle 25°, 85°\rangle_c$ fibre path; (d) $\Im\mathfrak{m}(\Omega)$, shell with a $\langle 25°, 85°\rangle_c$ fibre path.

Table 11
Critical free stream pressure p_{crit} and number of circumferential waves of the corresponding mode n_{crit} for shells with C-C and S-S boundary conditions.

Fibre path	C-C boundary conditions		S-S boundary conditions	
	n_{crit}	p_{crit} [Pa]	n_{crit}	p_{crit} [Pa]
$\psi = 55°$	20	1474	18	1065
$\langle 40°, 80°\rangle$	16	2368	14	2111
$\langle 25°, 85°\rangle_c$	16	3164	14	2870
$\langle 85°, 55°, 85°\rangle$	16	1816	15	1426
$\langle 85°, 45°, 85°\rangle_c$	17	2146	15	1708

the $\langle 40°, 80°\rangle$, the $\langle 25°, 85°\rangle_c$, the $\langle 85°, 55°, 85°\rangle$ and the $\langle 85°, 45°, 85°\rangle_c$ paths, and they can be compared with Figs. 5, 7, 8, 9 and 10 for their shell counterpart with C-C boundary conditions, respectively. The flutter mode shapes of each path, clamped and simply supported boundary conditions, differ not only because in the cylindrical shells with S-S edges slope is obvious at one of the extremities, but also because the flutter mode shapes of S-S shells have a different number of circumferential waves.

Furthermore, as an example, the $\Re\mathfrak{e}(\Omega)$ and $\Im\mathfrak{m}(\Omega)$ plot in relation to p_{∞} for the $\langle 40°, 80°\rangle$ path was obtained to compare the differences between a shell with C-C boundary conditions and S-S boundary conditions. The plots are present in Fig. 18. As it was previously stated, it is seen that, in this case, $\Re\mathfrak{e}(\Omega)$ becomes positive for a lower value of p_{∞} for a shell with simply supported edges. Analysing the variation of $\Im\mathfrak{m}(\Omega)$, it is seen that lower values for the vibration frequency under flutter were obtained for the shell with S-S boundary conditions. However, the values of p_{crit} decrease much less (about 12%) then the values of the wind-off natural frequencies of vibration (roughly 30%) with the change to softer boundaries. This is an alert to the fact that p_{crit} is not necessarily increased by making a structure stiffer; to delay couple mode flutter, it is important to increase the difference between the natural frequencies of vibration of the modes that interact.

By reviewing Table 11, it is seen that, even though there is a general decrease in the values of p_{crit} for the S-S boundary conditions, the curvilinear fibre paths still result in higher values of p_{crit} than the calculated constant angle path. This in spite of the fact that the true potential of the variable stiffness concept is not fully explored in Table 11, because, while a certain fibre path might be the ideal for a shell with C-C boundary conditions, it is not necessarily ideal path for a shell with S-S boundary conditions.

Table 12 contains the values of p_{crit} for 3 different linear angle variation paths of shells with C-C boundary conditions and S-S boundary conditions. These 3 paths have the same value for the T_0 parameter, but the T_1 parameter was slightly tweaked with the intent to understand if the highest value of p_{crit} is obtained for the same fibre path parameters in shells with different boundary conditions. A fuller parametric study

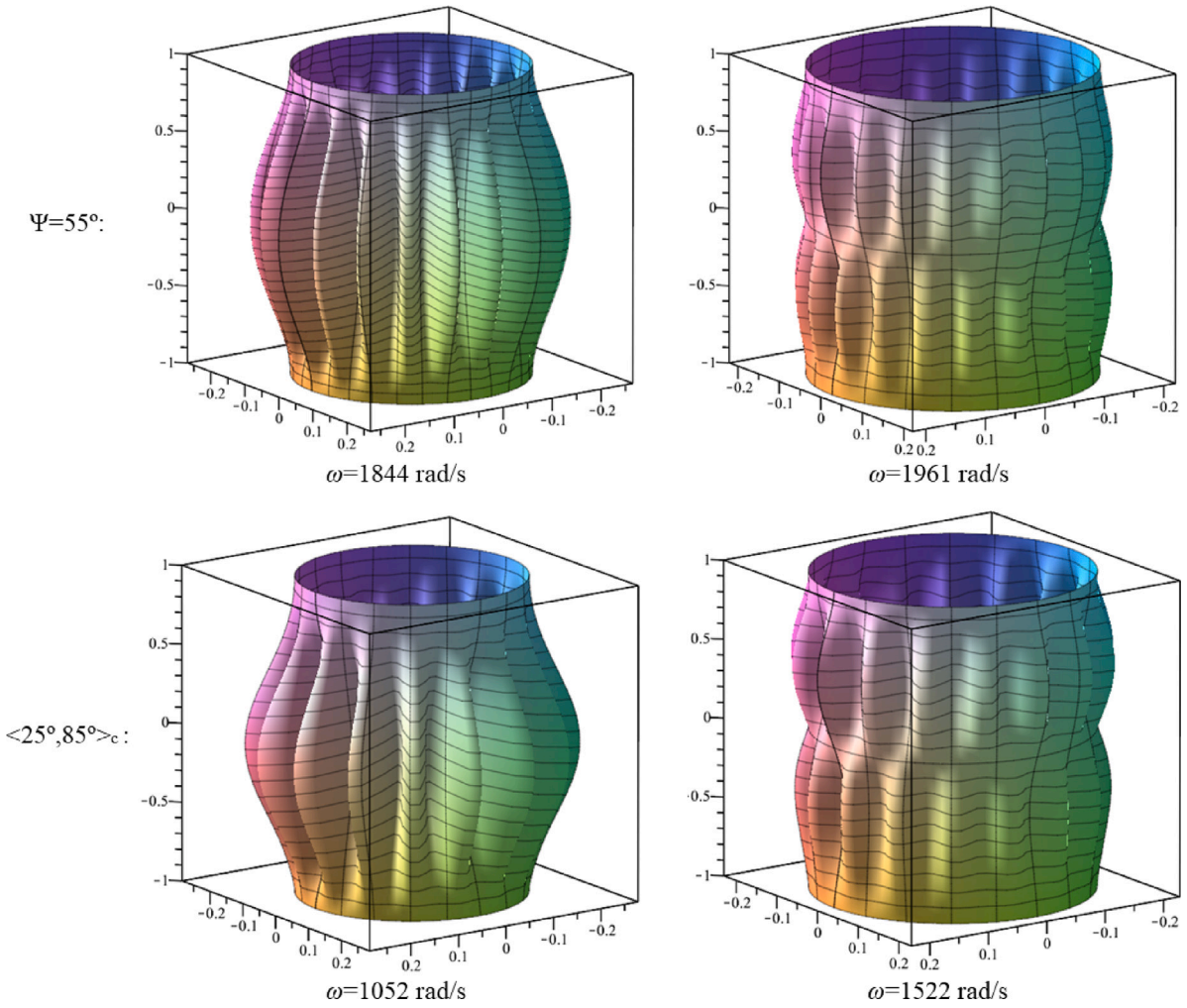

Fig. 12. Natural mode shapes of vibration and their corresponding natural frequencies and type of fibre path.

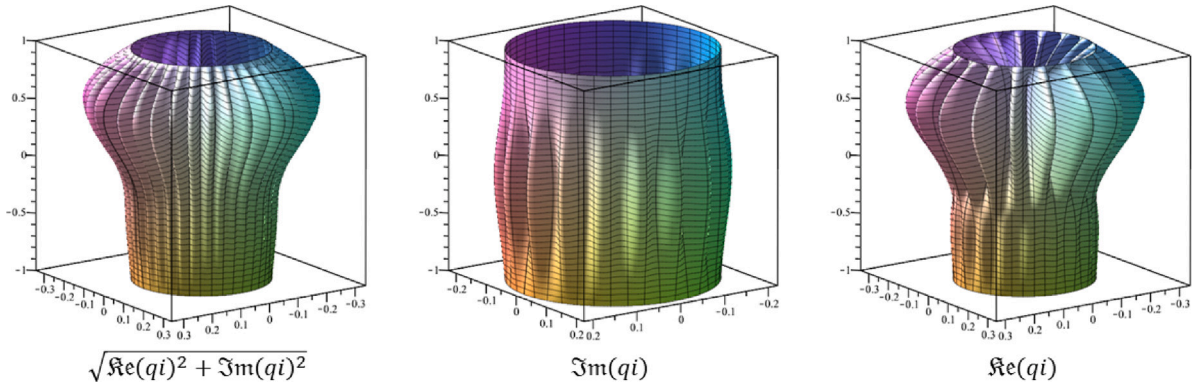

Fig. 13. Critical flutter mode shape of a CSCL shell with $T_0 = 55°$and S-S boundary conditions ($n_{crit} = 18$).

is not carried out, because it is not the goal of this section to find the fibre paths with the highest possible values of p_{crit} when boundary conditions are S-S, but – as said – to investigate how the boundary conditions affect the values of p_{crit} and associated flutter mode shapes.

Of the 3 tested paths, the highest value of p_{crit} was obtained with the ⟨40°, 80°⟩ tow path in the case of the shell with C-C boundary conditions, and it was obtained with the ⟨40°, 85°⟩ tow path in the case of the shell with S-S boundary conditions, thus showing that the ideal path to increase the value of p_{crit} is not the same for shells with different boundary conditions.

The various numerical tests show that the effect of the fibre path on the value of critical flutter pressure is complex to predict. The solution to improve the shells behaviour against flutter does not resume to trying to adjust the shells stiffness to avoid a certain flutter shape mode, since the critical flutter mode shape may change from fibre path to fibre path, or with a change in the boundary conditions.

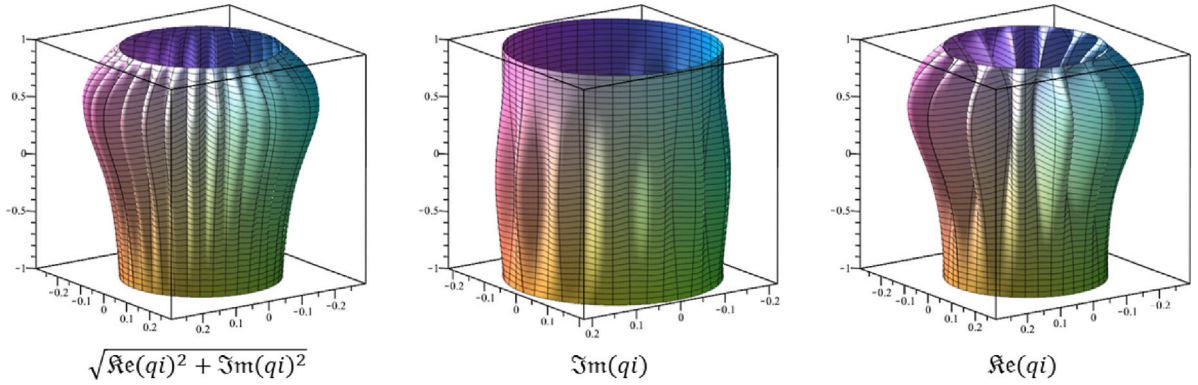

Fig. 14. Critical flutter mode shape of a VSCL shell with a $\langle 40°, 80° \rangle$ tow path and S-S boundary conditions ($n_{crit} = 14$).

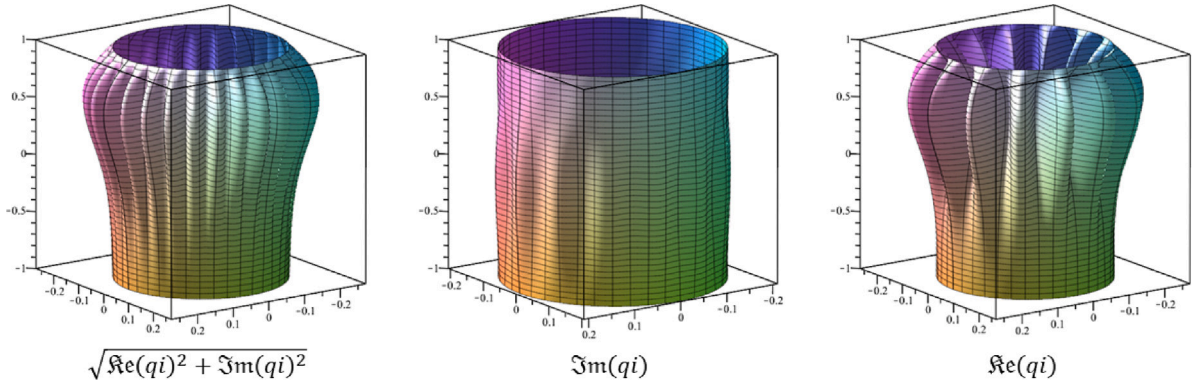

Fig. 15. Critical flutter mode shape of a VSCL shell with a $\langle 25°, 85° \rangle_c$ tow path and S-S boundary conditions ($n_{crit} = 14$).

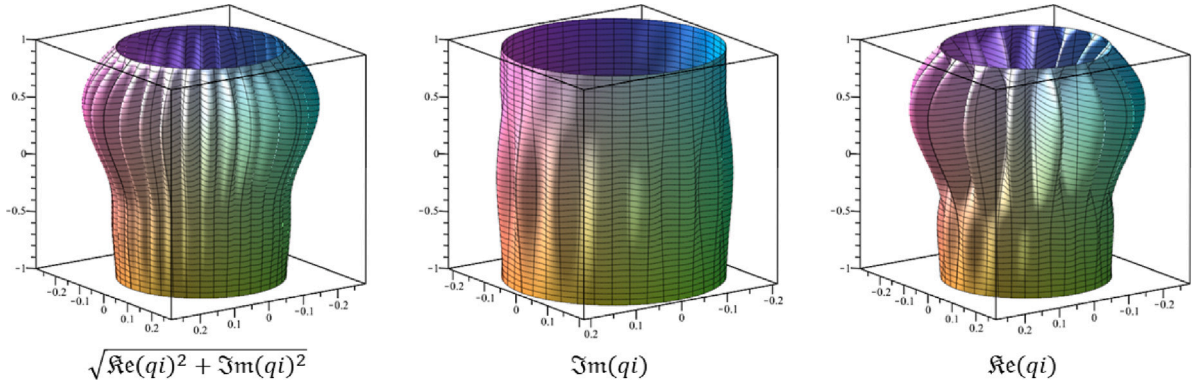

Fig. 16. Critical flutter mode shape of a VSCL shell with a $\langle 85°, 55°, 85° \rangle$ tow path and S-S boundary conditions ($n_{crit} = 15$).

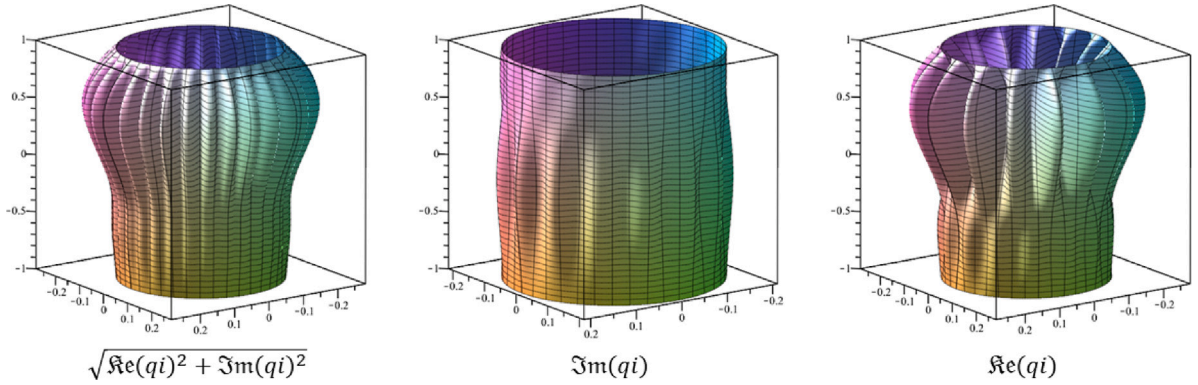

Fig. 17. Critical flutter mode shape of a VSCL shell with a $\langle 85°, 45°, 85° \rangle_c$ tow path and S-S boundary conditions ($n_{crit} = 15$).

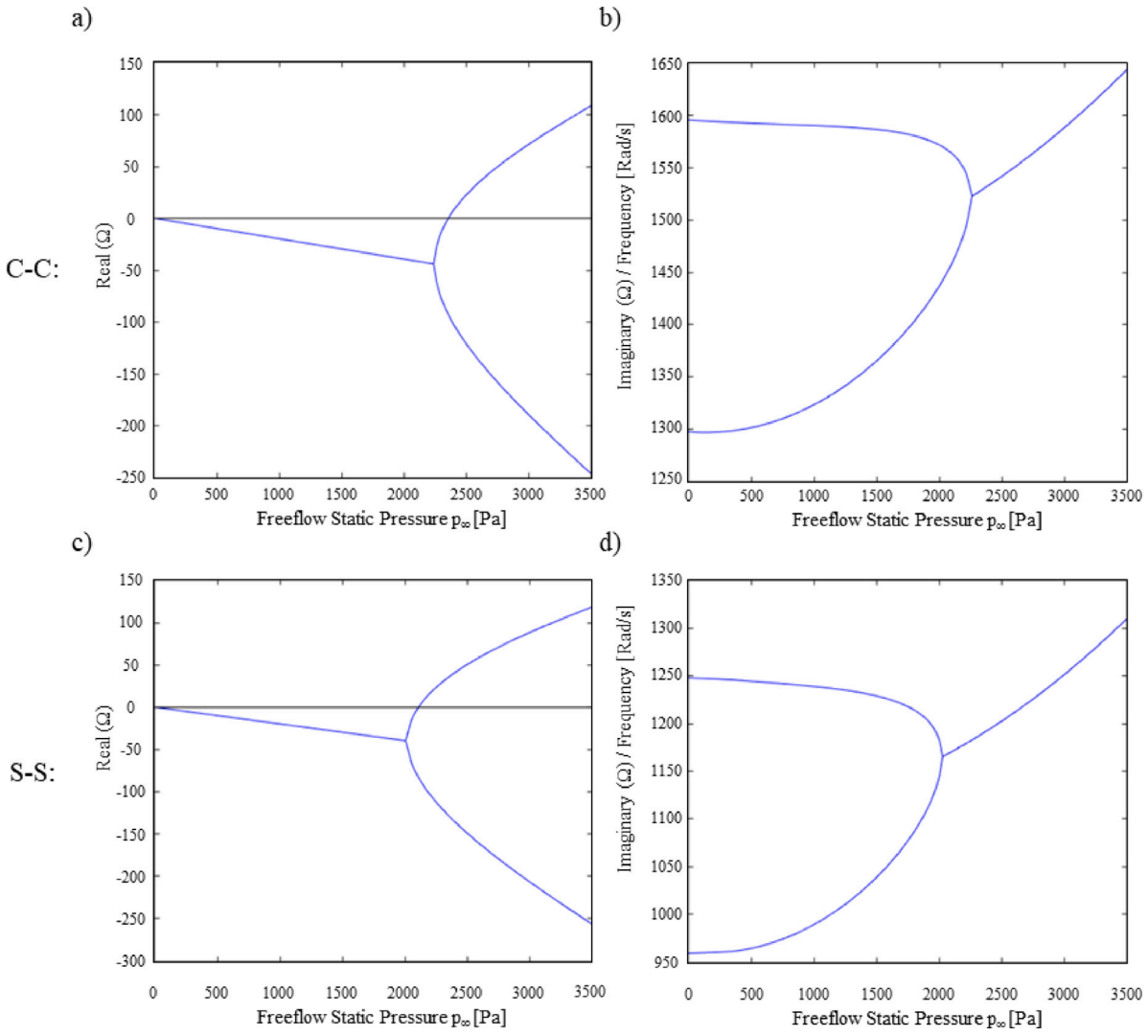

Fig. 18. Ω variation along p_∞ of the critical flutter mode and its corresponding coupled mode of a shell with a $\langle 40°, 80° \rangle$ tow path: (a) $\Re\mathfrak{e}(\Omega)$, C-C shell; (b) $\Im\mathfrak{m}(\Omega)$ C-C shell; (c) $\Re\mathfrak{e}(\Omega)$ S-S shell; (d) $\Im\mathfrak{m}(\Omega)$ S-S shell.

Table 12
Critical free stream pressure p_{crit} for shells with C-C and S-S boundary conditions and linear angle variation paths.

$\langle T_0, T_1 \rangle$		
Fibre path	C-C boundary conditions p_{crit} [Pa]	S-S boundary conditions p_{crit} [Pa]
$\langle 40°, 80° \rangle$	**2368**	2111
$\langle 40°, 85° \rangle$	2280	**2177**
$\langle 40°, 75° \rangle$	2328	2060

5. Conclusions

A model to determine the critical values of free stream static pressure, p_{crit}, on thin, variable stiffness composite circular cylindrical shells under supersonic flow was presented. In the numerical tests, constant stiffness (CSCL) and variable stiffness (VSCL) shells with four types of fibre paths were compared. The minimum turning radius manufacturing constraint was considered on the VSCL shells.

Firstly, shells clamped at both ends were analysed. CSCL shells were used as a benchmark to surpass by shells with curvilinear fibres. A relative increase of around 115% in relation to the constant stiffness shell with the highest critical pressure was obtained using curvilinear fibres. Higher values of critical pressure were obtained for fibre paths that have large differences between the fibre path parameters T_0 and T_1. The manufacturing curvature constraint proved to significantly limit the possible increase of p_{crit}; if this constraint can be reduced, even higher values of p_{crit} will be obtained.

VSCL with paths defined over one and two segments were examined. The manufacturing curvature constraint restricted more severely the choice of fibre path parameters in the two segment tow paths here implemented. Hence, even though these paths possess more complex geometries than one segment tow paths, lower maximum critical pressures were obtained for the tow paths with two segments as implemented here than for the ones with one segment.

For the same values of parameters T_0 and T_1, linear angle variation paths provide larger critical pressures than constant 'in-plane' curvature paths. However, both for one and two segment paths, higher critical pressures were obtained with constant curvature paths, rather than using linear angle variation. Again, this occurred because the linear angle variation path was more restricted by the curvature constraint.

The natural frequencies of vibration, without airflow, of the CSCL and VSCL shells for which p_{crit} achieved the highest values were compared. The difference between the values of the natural frequencies of the modes that couple when flutter occurs were higher in the shell with a curvilinear fibre path. This explains why using curvilinear fibres led to an increase of the value of p_{crit} .

Finally, shells with simply supported edges were compared with clamped shells. The change in boundary conditions not only altered the value of p_{crit}, but also the critical mode shape that achieved flutter first. The ideal fibre path for a shell with C-C boundary conditions may not be ideal for a shell with S-S boundary conditions, because the relation between the fibre orientation at the boundaries and the stiffness changes with the change in the boundary constrains.

In summary, it has been proven that variable stiffness composite laminates present a great capacity to postpone aeroelastic supersonic flutter of circular cylindrical shells. Nonetheless, as a follow up study, it would be interesting to implement an optimisation algorithm in conjunction with a more general fibre path definition, to increase even further the values of critical flutter pressure achieved using VSCL.

CRediT authorship contribution statement

Duarte Cachulo: Methodology, Software, Writing – original draft. **Hamed Akhavan:** Conceptualization, Methodology, Writing – review & editing, Supervision. **Pedro Ribeiro:** Conceptualization, Methodology, Writing – review & editing, Supervision, Project administration, Funding acquisition.

Declaration of competing interest

The authors declare the following financial interests/personal relationships which may be considered as potential competing interests: Pedro Ribeiro reports financial support was provided by Foundation for Science and Technology, FCT, Portugal.

Data availability

Data will be made available on request.

Acknowledgements

This research was carried out in the framework of project Nº 030348, POCI-01-0145-FEDER-030348, "Laminated composite panels reinforced with carbon nanotubes and curvilinear carbon fibres for enhanced vibration and flutter characteristics", funded by FEDER, through Programa Operacional Competitividade e Internacionalização – COMPETE 2020, and by National Funds (PIDDAC), through FCT/MCTES. The authors gratefully acknowledge the funding provided.

Appendix A

The stiffness and mass matrices can be written as

$$\mathbf{K}=\begin{bmatrix}\mathbf{K_{uu}} & \mathbf{K_{uv}} & \mathbf{K_{uw}}\\ \mathbf{K_{vu}} & \mathbf{K_{vv}} & \mathbf{K_{vw}}\\ \mathbf{K_{wu}} & \mathbf{K_{wv}} & \mathbf{K_{ww}}\end{bmatrix} \tag{30}$$

$$\mathbf{M}=\begin{bmatrix}\mathbf{M_{uu}} & \mathbf{0} & \mathbf{0}\\ \mathbf{0} & \mathbf{M_{vv}} & \mathbf{0}\\ \mathbf{0} & \mathbf{0} & \mathbf{M_{ww}}\end{bmatrix} \tag{31}$$

with

$$\begin{aligned}K_{uu,ko}=&\frac{2R}{l}\int_{-1}^{1}\frac{\mathrm{d}g_{ui}}{\mathrm{d}\xi}A_{11}\frac{\mathrm{d}g_{uj}}{\mathrm{d}\xi}\,\mathrm{d}\xi\int_{0}^{2\pi}h_{um}h_{un}\,\mathrm{d}\theta\\&-2\int_{-1}^{1}g_{ui}A_{16}\frac{\mathrm{d}g_{uj}}{\mathrm{d}\xi}\,\mathrm{d}\xi\int_{0}^{2\pi}h_{um}\frac{\mathrm{d}h_{un}}{\mathrm{d}\theta}\,\mathrm{d}\theta\\&+\frac{l}{2R}\int_{-1}^{1}g_{ui}A_{66}g_{uj}\,\mathrm{d}\xi\int_{0}^{2\pi}\frac{\mathrm{d}h_{um}}{\mathrm{d}\theta}\frac{\mathrm{d}h_{un}}{\mathrm{d}\theta}\,\mathrm{d}\theta\end{aligned} \tag{32}$$

$$\begin{aligned}K_{uv,ko}=&\frac{2R}{l}\int_{-1}^{1}\frac{\mathrm{d}g_{ui}}{\mathrm{d}\xi}A_{16}\frac{\mathrm{d}g_{vj}}{\mathrm{d}\xi}\,\mathrm{d}\xi\int_{0}^{2\pi}h_{um}h_{vn}\,\mathrm{d}\theta\\&-\int_{-1}^{1}g_{ui}(A_{12}+A_{66})\frac{\mathrm{d}g_{vj}}{\mathrm{d}\xi}\,\mathrm{d}\xi\int_{0}^{2\pi}h_{um}\frac{\mathrm{d}h_{vn}}{\mathrm{d}\theta}\,\mathrm{d}\theta\\&+\frac{l}{2R}\int_{-1}^{1}g_{ui}A_{26}g_{vj}\,\mathrm{d}\xi\int_{0}^{2\pi}\frac{\mathrm{d}h_{um}}{\mathrm{d}\theta}\frac{\mathrm{d}h_{vn}}{\mathrm{d}\theta}\,\mathrm{d}\theta\end{aligned} \tag{33}$$

$$\begin{aligned}K_{uw,ko}=&-\int_{-1}^{1}g_{ui}A_{12}\frac{\mathrm{d}f_{wj}}{\mathrm{d}\xi}\,\mathrm{d}\xi\int_{0}^{2\pi}h_{um}h_{wn}\,\mathrm{d}\theta\\&-\frac{l}{2R}\int_{-1}^{1}g_{ui}A_{26}f_{wj}\,\mathrm{d}\xi\int_{0}^{2\pi}h_{um}\frac{\mathrm{d}h_{wn}}{\mathrm{d}\theta}\,\mathrm{d}\theta\end{aligned} \tag{34}$$

$$\begin{aligned}K_{vu,ko}=&\frac{2R}{l}\int_{-1}^{1}\frac{\mathrm{d}g_{vi}}{\mathrm{d}\xi}A_{16}\frac{\mathrm{d}g_{uj}}{\mathrm{d}\xi}\,\mathrm{d}\xi\int_{0}^{2\pi}h_{vm}h_{un}\,\mathrm{d}\theta\\&-\int_{-1}^{1}g_{vi}(A_{12}+A_{66})\frac{\mathrm{d}g_{uj}}{\mathrm{d}\xi}\,\mathrm{d}\xi\int_{0}^{2\pi}h_{vm}\frac{\mathrm{d}h_{un}}{\mathrm{d}\theta}\,\mathrm{d}\theta\\&+\frac{l}{2R}\int_{-1}^{1}g_{vi}A_{26}g_{uj}\,\mathrm{d}\xi\int_{0}^{2\pi}\frac{\mathrm{d}h_{vm}}{\mathrm{d}\theta}\frac{\mathrm{d}h_{un}}{\mathrm{d}\theta}\,\mathrm{d}\theta\end{aligned} \tag{35}$$

$$\begin{aligned}K_{vv,ko}=&\frac{2R}{l}\int_{-1}^{1}\frac{\mathrm{d}g_{vi}}{\mathrm{d}\xi}A_{66}\frac{\mathrm{d}g_{vj}}{\mathrm{d}\xi}\,\mathrm{d}\xi\int_{0}^{2\pi}h_{vm}h_{vn}\,\mathrm{d}\theta\\&-2\int_{-1}^{1}g_{vi}A_{26}\frac{\mathrm{d}g_{vj}}{\mathrm{d}\xi}\,\mathrm{d}\xi\int_{0}^{2\pi}h_{vm}\frac{\mathrm{d}h_{vn}}{\mathrm{d}\theta}\,\mathrm{d}\theta\\&+\frac{l}{2R}\int_{-1}^{1}g_{vi}A_{22}g_{vj}\,\mathrm{d}\xi\int_{0}^{2\pi}\frac{\mathrm{d}h_{vm}}{\mathrm{d}\theta}\frac{\mathrm{d}h_{vn}}{\mathrm{d}\theta}\,\mathrm{d}\theta\\&+\frac{2}{lR}\int_{-1}^{1}\frac{\mathrm{d}g_{vi}}{\mathrm{d}\xi}D_{66}\frac{\mathrm{d}g_{vj}}{\mathrm{d}\xi}\,\mathrm{d}\xi\int_{0}^{2\pi}h_{vm}h_{vn}\,\mathrm{d}\theta\\&-\frac{2}{R^2}\int_{-1}^{1}g_{vi}D_{26}\frac{\mathrm{d}g_{vj}}{\mathrm{d}\xi}\,\mathrm{d}\xi\int_{0}^{2\pi}h_{vm}\frac{\mathrm{d}h_{vn}}{\mathrm{d}\theta}\,\mathrm{d}\theta\\&+\frac{l}{2R^3}\int_{-1}^{1}g_{vi}D_{22}g_{vj}\,\mathrm{d}\xi\int_{0}^{2\pi}\frac{\mathrm{d}h_{vm}}{\mathrm{d}\theta}\frac{\mathrm{d}h_{vn}}{\mathrm{d}\theta}\,\mathrm{d}\theta\end{aligned} \tag{36}$$

$$\begin{aligned}K_{vw,ko}=&-\frac{4}{l^2}\int_{-1}^{1}\frac{\mathrm{d}g_{vi}}{\mathrm{d}\xi}D_{16}\frac{\mathrm{d}^2f_{wj}}{\mathrm{d}\xi^2}\,\mathrm{d}\xi\int_{0}^{2\pi}h_{vm}h_{wn}\,\mathrm{d}\theta\\&-\frac{l}{2R^3}\int_{-1}^{1}g_{vi}D_{22}f_{wj}\,\mathrm{d}\xi\int_{0}^{2\pi}\frac{\mathrm{d}h_{vm}}{\mathrm{d}\theta}\frac{\mathrm{d}^2h_{wn}}{\mathrm{d}\theta^2}\,\mathrm{d}\theta\\&-\frac{3}{R^2}\int_{-1}^{1}g_{vi}D_{26}\frac{\mathrm{d}f_{wj}}{\mathrm{d}\xi}\,\mathrm{d}\xi\int_{0}^{2\pi}\frac{\mathrm{d}h_{vm}}{\mathrm{d}\theta}\frac{\mathrm{d}h_{wn}}{\mathrm{d}\theta}\,\mathrm{d}\theta\\&-\frac{2}{lR}\int_{-1}^{1}\frac{\mathrm{d}g_{vi}}{\mathrm{d}\xi}(D_{12}+2D_{66})\frac{\mathrm{d}f_{wj}}{\mathrm{d}\xi}\,\mathrm{d}\xi\int_{0}^{2\pi}h_{vm}\frac{\mathrm{d}h_{wn}}{\mathrm{d}\theta}\,\mathrm{d}\theta\\&-\int_{-1}^{1}g_{vi}A_{26}\frac{\mathrm{d}f_{wj}}{\mathrm{d}\xi}\,\mathrm{d}\xi\int_{0}^{2\pi}h_{vm}h_{wn}\,\mathrm{d}\theta\\&-\frac{l}{2R}\int_{-1}^{1}g_{vi}A_{22}f_{wj}\,\mathrm{d}\xi\int_{0}^{2\pi}h_{vm}\frac{\mathrm{d}h_{wn}}{\mathrm{d}\theta}\,\mathrm{d}\theta\end{aligned} \tag{37}$$

$$\begin{aligned}K_{wu,ko}=&\int_{-1}^{1}f_{wi}A_{12}\frac{\mathrm{d}g_{uj}}{\mathrm{d}\xi}\,\mathrm{d}\xi\int_{0}^{2\pi}h_{wm}h_{un}\,\mathrm{d}\theta\\&+\frac{l}{2R}\int_{-1}^{1}f_{wi}A_{26}g_{uj}\,\mathrm{d}\xi\int_{0}^{2\pi}h_{wm}\frac{\mathrm{d}h_{un}}{\mathrm{d}\theta}\,\mathrm{d}\theta\end{aligned} \tag{38}$$

$$\begin{aligned}K_{wv,ko}=&\frac{4}{l^2}\int_{-1}^{1}\frac{\mathrm{d}f_{wi}}{\mathrm{d}\xi}D_{16}\frac{\mathrm{d}^2g_{vj}}{\mathrm{d}\xi^2}\,\mathrm{d}\xi\int_{0}^{2\pi}h_{wm}h_{vn}\,\mathrm{d}\theta\\&+\frac{l}{2R^3}\int_{-1}^{1}f_{wi}D_{22}g_{vj}\,\mathrm{d}\xi\int_{0}^{2\pi}\frac{\mathrm{d}h_{wm}}{\mathrm{d}\theta}\frac{\mathrm{d}^2h_{vn}}{\mathrm{d}\theta^2}\,\mathrm{d}\theta\\&+\frac{3}{R^2}\int_{-1}^{1}f_{wi}D_{26}\frac{\mathrm{d}g_{vj}}{\mathrm{d}\xi}\,\mathrm{d}\xi\int_{0}^{2\pi}\frac{\mathrm{d}h_{wm}}{\mathrm{d}\theta}\frac{\mathrm{d}h_{vn}}{\mathrm{d}\theta}\,\mathrm{d}\theta\\&+\frac{2}{lR}\int_{-1}^{1}\frac{\mathrm{d}f_{wi}}{\mathrm{d}\xi}(D_{12}+2D_{66})\frac{\mathrm{d}g_{vj}}{\mathrm{d}\xi}\,\mathrm{d}\xi\int_{0}^{2\pi}h_{wm}\frac{\mathrm{d}h_{vn}}{\mathrm{d}\theta}\,\mathrm{d}\theta\\&+\int_{-1}^{1}f_{wi}A_{26}\frac{\mathrm{d}g_{vj}}{\mathrm{d}\xi}\,\mathrm{d}\xi\int_{0}^{2\pi}h_{wm}h_{vn}\,\mathrm{d}\theta\\&+\frac{l}{2R}\int_{-1}^{1}f_{wi}A_{22}g_{vj}\,\mathrm{d}\xi\int_{0}^{2\pi}h_{wm}\frac{\mathrm{d}h_{vn}}{\mathrm{d}\theta}\,\mathrm{d}\theta\end{aligned} \tag{39}$$

$$
\begin{aligned}
K_{ww,ko} = {} & \frac{8R}{l^3}\int_{-1}^{1}\frac{\mathrm{d}^2 f_{wi}}{\mathrm{d}\xi^2}D_{11}\frac{\mathrm{d}^2 f_{wj}}{\mathrm{d}\xi^2}\,\mathrm{d}\xi\int_0^{2\pi}h_{wm}h_{wn}\,\mathrm{d}\theta \\
& -\frac{16}{l^2}\int_{-1}^{1}\frac{\mathrm{d}f_{wi}}{\mathrm{d}\xi}D_{16}\frac{\mathrm{d}^2 f_{wj}}{\mathrm{d}\xi^2}\,\mathrm{d}\xi\int_0^{2\pi}h_{wm}\frac{\mathrm{d}h_{wn}}{\mathrm{d}\theta}\,\mathrm{d}\theta \\
& +\frac{4}{lR}\int_{-1}^{1}\frac{\mathrm{d}f_{wi}}{\mathrm{d}\xi}(D_{12}+2D_{66})\frac{\mathrm{d}f_{wj}}{\mathrm{d}\xi}\,\mathrm{d}\xi\int_0^{2\pi}\frac{\mathrm{d}h_{wm}}{\mathrm{d}\theta}\frac{\mathrm{d}h_{wn}}{\mathrm{d}\theta}\,\mathrm{d}\theta \\
& -\frac{4}{R^2}\int_{-1}^{1}f_{wi}D_{26}\frac{\mathrm{d}f_{wj}}{\mathrm{d}\xi}\,\mathrm{d}\xi\int_0^{2\pi}\frac{\mathrm{d}h_{wm}}{\mathrm{d}\theta}\frac{\mathrm{d}^2 h_{wn}}{\mathrm{d}\theta^2}\,\mathrm{d}\theta \\
& +\frac{l}{2R^3}\int_{-1}^{1}f_{wi}D_{22}f_{wj}\,\mathrm{d}\xi\int_0^{2\pi}\frac{\mathrm{d}^2 h_{wm}}{\mathrm{d}\theta^2}\frac{\mathrm{d}^2 h_{wn}}{\mathrm{d}\theta^2}\,\mathrm{d}\theta \\
& +\frac{l}{2R}\int_{-1}^{1}f_{wi}A_{22}f_{wj}\,\mathrm{d}\xi\int_0^{2\pi}h_{wm}h_{wn}\,\mathrm{d}\theta
\end{aligned}
\tag{40}
$$

$$
M_{uu,ko} = \frac{lR}{2}\rho h\int_{-1}^{1}g_{ui}g_{uj}\,\mathrm{d}\xi\int_0^{2\pi}h_{um}h_{un}\,\mathrm{d}\theta \tag{41}
$$

$$
M_{vv,ko} = \frac{lR}{2}\rho h\int_{-1}^{1}g_{vi}g_{vj}\,\mathrm{d}\xi\int_0^{2\pi}h_{vm}h_{vn}\,\mathrm{d}\theta \tag{42}
$$

$$
M_{ww,ko} = \frac{lR}{2}\rho h\int_{-1}^{1}f_{wi}f_{wj}\,\mathrm{d}\xi\int_0^{2\pi}h_{wm}h_{wn}\,\mathrm{d}\theta \tag{43}
$$

By way of example, Eq. (32) is used to explain the relations between the diverse indexes. Here, symbols k and o identify a term of the matrix; both vary from 1 to $p_m \cdot p_t$. Symbols i and j vary from 1 to p_m according to the following rules

$$
i = \mathrm{Int}\frac{k-1}{p_t} + 1 \tag{44}
$$

$$
j = \mathrm{Int}\frac{o-1}{p_t} + 1 \tag{45}
$$

where Int(•) is an operator that rounds down a number (a rational number, in this case) to an integer. Symbols m and n vary from 1 to p_t according to

$$
m = k - p_t \cdot (i-1) \tag{46}
$$

$$
n = o - p_t \cdot (j-1) \tag{47}
$$

Appendix B

By applying Galerkin's method, the terms on the right-hand side of Eq. (13) lead to the following matrices that are due to the fluid–structure interaction,

$$
\mathbf{F}_{\mathbf{Piston\,1}} = \begin{bmatrix}\mathbf{0} & \mathbf{0} & \mathbf{0}\\ \mathbf{0} & \mathbf{0} & \mathbf{0}\\ \mathbf{0} & \mathbf{0} & \mathbf{F_s}\end{bmatrix}, \mathbf{F}_{\mathbf{Piston\,2}} = \begin{bmatrix}\mathbf{0} & \mathbf{0} & \mathbf{0}\\ \mathbf{0} & \mathbf{0} & \mathbf{0}\\ \mathbf{0} & \mathbf{0} & \mathbf{F_u}\end{bmatrix} \tag{48}
$$

with

$$
\begin{aligned}
F_{s,ko} = {} & \frac{\gamma p_\infty M^2}{\sqrt{M^2-1}}\cdot R\int_{-1}^{1}f_{wi}\frac{\mathrm{d}f_{wj}}{\mathrm{d}\xi}\,\mathrm{d}\xi\int_0^{2\pi}h_{wm}h_{wn}\,\mathrm{d}\theta \\
& -\frac{\gamma p_\infty M^2}{\sqrt{M^2-1}}\cdot\frac{1}{2R\sqrt{M^2-1}}\cdot\frac{lR}{2}\int_{-1}^{1}f_{wi}f_{wj}\,\mathrm{d}\xi\int_0^{2\pi}h_{wm}h_{wn}\,\mathrm{d}\theta
\end{aligned}
\tag{49}
$$

and

$$
\begin{aligned}
F_{u,ko} = {} & \frac{\gamma p_\infty M^2}{\sqrt{M^2-1}}\cdot\frac{1}{M a_\infty}\cdot\left(\frac{M^2-2}{M^2-1}\right) \\
& \cdot\frac{lR}{2}\int_{-1}^{1}f_{wi}f_{wj}\,\mathrm{d}\xi\int_0^{2\pi}h_{wm}h_{wn}\,\mathrm{d}\theta
\end{aligned}
\tag{50}
$$

where indexes i, j, k, m, n and o vary as described in Appendix A.

References

[1] Qatu MS. Vibration of laminated shells and plates. Elsevier; 2004.

[2] Dowell EH. A modern course in aeroelasticity. 6th ed.. Cham, Switzerland: Springer; 2022.

[3] Ghiasi H, Fayazbakhsh K, Pasini D, Lessard L. Optimum stacking sequence design of composite materials Part II: Variable stiffness design. Compos Struct 2010;93(1):1–13. http://dx.doi.org/10.1016/j.compstruct.2010.06.001, URL https://www.sciencedirect.com/science/article/pii/S0263822310001947.

[4] Ribeiro P, Akhavan H, Teter A, Warminski J. A review on the mechanical behaviour of curvilinear fibre composite laminated panels. J Compos Mater 2014;48(22):2761–77. http://dx.doi.org/10.1177/0021998313502066.

[5] Albazzan MA, Harik R, Tatting BF, Gürdal Z. Efficient design optimization of non-conventional laminated composites using lamination parameters: A state of the art. Compos Struct 2019;209:362–74. http://dx.doi.org/10.1016/j.compstruct.2018.10.095.

[6] Aragh BS, Farahani EB, Xu B, Ghasemnejad H, Mansur W. Manufacturable insight into modelling and design considerations in fibre-steered composite laminates: State of the art and perspective. Comput Methods Appl Mech Engrg 2021;379:113752. http://dx.doi.org/10.1016/j.cma.2021.113752.

[7] Lozano GG, Tiwari A, Turner C, Astwood S. A review on design for manufacture of variable stiffness composite laminates. Proc Inst Mech Eng B 2016;230(6):981–92. http://dx.doi.org/10.1177/0954405415600012.

[8] Heinecke F, Willberg C. Manufacturing-induced imperfections in composite parts manufactured via automated fiber placement. J Compos Sci 2019;3(2):56. http://dx.doi.org/10.3390/jcs3020056.

[9] Tatting BF. Analysis and design of variable stiffness composite cylinders (Ph.D. thesis), Virginia Tech; 1998.

[10] Blom AW, Setoodeh S, Hol JM, Gürdal Z. Design of variable-stiffness conical shells for maximum fundamental eigenfrequency. Comput Struct 2008;86(9):870–8. http://dx.doi.org/10.1016/j.compstruc.2007.04.020, URL https://www.sciencedirect.com/science/article/pii/S0045794907001630, Composites.

[11] Blom AW. Structural performance of fiber-placed, variable-stiffness composite conical and cylindrical shells (Ph.D. thesis), Delft University of Technology; 2010.

[12] Blom AW, Lopes CS, Kromwijk PJ, Gurdal Z, Camanho PP. A theoretical model to study the influence of tow-drop areas on the stiffness and strength of variable-stiffness laminates. J Compos Mater 2009. http://dx.doi.org/10.1177/0021998308097675.

[13] Wu KC. Design and analysis of tow-steered composite shells using fiber placement. In: Proceedings of American society for composites 23rd annual technical conference. Memphis, TN; 2008, p. 125–42.

[14] Wu K, Tatting B, Smith B, Stevens R, Occhipinti G, Swift J, Achary D, Thornburgh R. Design and manufacturing of tow-steered composite shells using fiber placement. In: 50th AIAA/ASME/ASCE/AHS/ASC structures, structural dynamics, and materials conference. 2009, p. 2700. http://dx.doi.org/10.2514/6.2009-2700.

[15] Pan H, Qu W, Yang D, Huang Q, Li J, Ke Y. Design and optimization of variable stiffness composite cylinders with the consideration of manufacturing interaction. Appl Compos Mater 2022;1–25. http://dx.doi.org/10.1007/s10443-021-10007-y.

[16] Wu KC, Stanford BK, Hrinda GA, Wang Z, Martin RA, Kim HA. Structural assessment of advanced tow-steered shells. In: 54th AIAA/ASME/ASCE/AHS/ASC structures, structural dynamics, and materials conference. 2013, p. 1769.

[17] Nik MA. Surrogate-based multi-objective optimization of variable stiffness composites with embedded defects induced by automated fiber placement (Ph.D. thesis), Canada: McGill University; 2014.

[18] Rouhi M, Ghayoor H, Fortin-Simpson J, Zacchia TT, Hoa SV, Hojjati M. Design, manufacturing, and testing of a variable stiffness composite cylinder. Compos Struct 2018;184:146–52. http://dx.doi.org/10.1016/j.compstruct.2017.09.090.

[19] Labans E, Bisagni C. Buckling and free vibration study of variable and constant-stiffness cylindrical shells. Compos Struct 2019;210:446–57. http://dx.doi.org/10.1016/j.compstruct.2018.11.061.

[20] Almeida JHS, Bittrich L, Jansen E, Tita V, Spickenheuer A. Buckling optimization of composite cylinders for axial compression: A design methodology considering a variable-axial fiber layout. Compos Struct 2019;222:110928. http://dx.doi.org/10.1016/j.compstruct.2019.110928, URL https://www.sciencedirect.com/science/article/pii/S0263822318346257.

[21] Ribeiro P. Linear modes of vibration of cylindrical shells in composite laminates reinforced by curvilinear fibres. J Vib Control 2016;22(20):4141–58. http://dx.doi.org/10.1177/1077546315571661.

[22] Ribeiro P, Stoykov S. Forced periodic vibrations of cylindrical shells in laminated composites with curvilinear fibres. Compos Struct 2015;131:462–78. http://dx.doi.org/10.1016/j.compstruct.2015.05.050, URL https://www.sciencedirect.com/science/article/pii/S0263822315004249.

[23] Babuška I, Suri M. The p and h-p versions of the finite element method, basic principles and properties. SIAM Rev 1994;36(4):578–632.

[24] Sciascia G, Oliveri V, Milazzo A, Weaver PM. Ritz solution for transient analysis of variable-stiffness shell structures. AIAA J 2020;58(4):1796–810. http://dx.doi.org/10.2514/1.J058686.

[25] Sciascia G, Oliveri V, Weaver PM. Dynamic analysis of prestressed variable stiffness composite shell structures. Thin-Walled Struct 2022;175:109193. http://dx.doi.org/10.1016/j.tws.2022.109193, URL https://www.sciencedirect.com/science/article/pii/S0263823122001707.

[26] Sciascia G, Oliveri V, Weaver PM. Eigenfrequencies of prestressed variable stiffness composite shells. Compos Struct 2021;270:114019. http://dx.doi.org/10.1016/j.compstruct.2021.114019, URL https://www.sciencedirect.com/science/article/pii/S0263822321004797.

[27] Guimarães TAM, Castro SGP, Cesnik CES, Rade DA. Supersonic flutter and buckling optimization of tow-steered composite plates. AIAA J 2018;57(1):397–407. http://dx.doi.org/10.2514/1.J057282.

[28] Khalafi V, Fazilati J. Supersonic panel flutter of variable stiffness composite laminated skew panels subjected to yawed flow by using NURBS-based isogeometric approach. J Fluids Struct 2018;82:198–214. http://dx.doi.org/10.1016/j.jfluidstructs.2018.07.002.

[29] Stodieck O, Cooper JE, Weaver PM, Kealy P. Improved aeroelastic tailoring using tow-steered composites. Compos Struct 2013;106:703–15. http://dx.doi.org/10.1016/j.compstruct.2013.07.023.

[30] Stodieck O, Cooper JE, Weaver P, Kealy P. Optimization of tow-steered composite wing laminates for aeroelastic tailoring. AIAA J 2015;53(8):2203–15. http://dx.doi.org/10.2514/1.J053599.

[31] Stanford BK, Jutte CV. Comparison of curvilinear stiffeners and tow steered composites for aeroelastic tailoring of aircraft wings. Comput Struct 2017;183:48–60. http://dx.doi.org/10.1016/j.compstruc.2017.01.010.

[32] Akhavan H, Ribeiro P. Aeroelasticity of composite plates with curvilinear fibres in supersonic flow. Compos Struct 2018;194:335–44. http://dx.doi.org/10.1016/j.compstruct.2018.03.101.

[33] Akhavan H, Ribeiro P. Reduced-order models for nonlinear flutter of composite laminates with curvilinear fibers. AIAA J 2019;57(7):3026–39. http://dx.doi.org/10.2514/1.J057755.

[34] Akhavan H, Ribeiro P. Stability and bifurcations in oscillations of composite laminates with curvilinear fibres under a supersonic airflow. Nonlinear Dynam 2021;103(4):3037–58. http://dx.doi.org/10.1007/s11071-020-05838-6.

[35] Akhavan H, Ribeiro P. Nonlinear flutter of composite laminates with curvilinear fibres using a full linearized aerodynamic theory. J Fluids Struct 2022;115:103756. http://dx.doi.org/10.1016/j.jfluidstructs.2022.103756, URL https://www.sciencedirect.com/science/article/pii/S0889974622001487.

[36] Camacho P, Akhavan H, Ribeiro P. Linear aeroelastic analysis of cantilever hybrid composite laminated plates with curvilinear fibres and carbon nanotubes. Compos Struct 2021;266:113765. http://dx.doi.org/10.1016/j.compstruct.2021.113765.

[37] Olson MD, Fung Y. Supersonic flutter of circular cylindrical shells subjected to internal pressure and axial compression. AIAA J 1966;4(5):858–64.

[38] Evensen DA, Olson MD. Nonlinear flutter of a circular cylindrical shell in supersonic flow; No. NASA-TN-D-4265. Tech. rep., Langley Research Center; 1967.

[39] Carter L, Stearman R. Some aspects of cylindrical shell panel flutter. AIAA J 1968;6(1):37–43.

[40] Bismarck-Nasr MN. Finite element method applied to the supersonic flutter of circular cylindrical shells. Internat J Numer Methods Engrg 1976;10(2):423–35.

[41] Ganapathi M, Varadan T, Jijen J. Field-consistent element applied to flutter analysis of circular cylindrical shells. J Sound Vib 1994;171(4):509–27. http://dx.doi.org/10.1006/jsvi.1994.1137.

[42] Amabili M, Pellicano F. Multimode approach to nonlinear supersonic flutter of imperfect circular cylindrical shells. J Appl Mech 2002;69(2):117–29. http://dx.doi.org/10.1115/1.1435366.

[43] Sabri F, Lakis AA. Finite element method applied to supersonic flutter of circular cylindrical shells. AIAA J 2010;48(1):73–81. http://dx.doi.org/10.2514/1.39580.

[44] Amabili M. Nonlinear vibrations and stability of shells and plates. Cambridge University Press; 2008, http://dx.doi.org/10.1017/CBO9780511619694.

[45] Mahmoudkhani S, Sadeghmanesh M, Haddadpour H. Aero-thermo-elastic stability analysis of sandwich viscoelastic cylindrical shells in supersonic airflow. Compos Struct 2016;147:185–96. http://dx.doi.org/10.1016/j.compstruct.2016.03.020.

[46] Chen J, Li Q-S. Nonlinear aeroelastic flutter and dynamic response of composite laminated cylindrical shell in supersonic air flow. Compos Struct 2017;168:474–84. http://dx.doi.org/10.1016/j.compstruct.2017.02.019.

[47] Avramov K, Chernobryvko M, Uspensky B, Seitkazenova K, Myrzaliyev D. Self-sustained vibrations of functionally graded carbon nanotubes-reinforced composite cylindrical shells in supersonic flow. Nonlinear Dynam 2019;98(3):1853–76. http://dx.doi.org/10.1007/s11071-019-05292-z.

[48] Wei J, Song Z, Li F. Superior aeroelastic behaviors of axially functional graded cylindrical shells in supersonic airflow. J Fluids Struct 2020;96. http://dx.doi.org/10.1016/j.jfluidstructs.2020.103027.

[49] Fayazbakhsh K, Nik MA, Pasini D, Lessard L. Defect layer method to capture effect of gaps and overlaps in variable stiffness laminates made by Automated Fiber Placement. Compos Struct 2013;97:245–51. http://dx.doi.org/10.1016/j.compstruct.2012.10.031.

[50] Vertonghen L, Castro S. Modelling of fibre steered plates with coupled thickness variation from overlapping continuous tows. Compos Struct 2021;268. http://dx.doi.org/10.1016/j.compstruct.2021.113933.

[51] Jansen E. The effect of geometric imperfections on the vibrations of anisotropic cylindrical shells. Thin-Walled Struct 2007;45:274–82. http://dx.doi.org/10.1016/j.tws.2007.02.014.

[52] Olson MD, Fung YC. Comparing theory and experiment for the supersonic flutter of circular cylindrical shells. AIAA J 1967;5(10):1849–56. http://dx.doi.org/10.2514/3.4315.

[53] Leissa AW. Vibration of shells. Scientific and Technical Information Office, National Aeronautics and Space Administration; 1973.

[54] Reddy JN. Mechanics of laminated composite plates and shells: Theory and analysis. CRC Press; 2003.

[55] Ashley H, Zartarian G. Piston theory-a new aerodynamic tool for the aeroelastician. J Aeronaut Sci 1956;23(12):1109–18.

[56] Barr GW, Stearman RO. Influence of a supersonic flowfield on the elastic stability of cylindrical shells. AIAA J 1970;8(6):993–1000.

[57] Amabili M, Pellicano F. Nonlinear supersonic flutter of circular cylindrical shells. AIAA J 2001;39(4):564–73. http://dx.doi.org/10.2514/2.1365.

[58] Han W, Petyt M, Hsiao K-M. An investigation into geometrically nonlinear analysis of rectangular laminated plates using the hierarchical finite element method. Finite Elem Anal Des 1994;18(1):273–88. http://dx.doi.org/10.1016/0168-874X(94)90107-4, URL https://www.sciencedirect.com/science/article/pii/0168874X94901074.

[59] Bardell N, Dunsdon J, Langley RS. Free and forced vibration analysis of thin, laminated, cylindrically curved panels. Compos Struct 1997;38(1–4):453–62. http://dx.doi.org/10.1016/S0263-8223(97)00080-9.

[60] Houmat A. An alternative hierarchical finite element formulation applied to plate vibrations. J Sound Vib 1997;206(2):201–15. http://dx.doi.org/10.1006/jsvi.1997.1076.

[61] Ribeiro P, Cochelin B, Bellizzi S. Non-linear vibrations of deep cylindrical shells by the p-version finite element. Shock Vib 2010;17:21–7. http://dx.doi.org/10.3233/SAV-2010-0495.

[62] Bardell N. The application of symbolic computing to the hierarchical finite element method. Internat J Numer Methods Engrg 1989;28(5):1181–204.

[63] Pellicano F. Vibrations of circular cylindrical shells: theory and experiments. J Sound Vib 2007;303(1–2):154–70.

[64] Song X, Han Q, Zhai J. Vibration analyses of symmetrically laminated composite cylindrical shells with arbitrary boundaries conditions via Rayleigh–Ritz method. Compos Struct 2015;134:820–30. http://dx.doi.org/10.1016/j.compstruct.2015.08.134.

[65] Qin Z, Chu F, Zu J. Free vibrations of cylindrical shells with arbitrary boundary conditions: a comparison study. Int J Mech Sci 2017;133:91–9. http://dx.doi.org/10.1016/j.ijmecsci.2017.08.012.

[66] Xie X, Jin G, Yan Y, Shi S, Liu Z. Free vibration analysis of composite laminated cylindrical shells using the Haar wavelet method. Compos Struct 2014;109:169–77. http://dx.doi.org/10.1016/j.compstruct.2013.10.058.

[67] Jin G, Ye T, Chen Y, Su Z, Yan Y. An exact solution for the free vibration analysis of laminated composite cylindrical shells with general elastic boundary conditions. Compos Struct 2013;106:114–27. http://dx.doi.org/10.1016/j.compstruct.2013.06.002.

[68] Lam K, Loy C. Analysis of rotating laminated cylindrical shells by different thin shell theories. J Sound Vib 1995;186(1):23–35.

[69] Zhang X. Vibration analysis of cross-ply laminated composite cylindrical shells using the wave propagation approach. Appl Acoust 2001;62(11):1221–8.

[70] Timarci T, Soldatos K. Vibrations of angle-ply laminated circular cylindrical shells subjected to different sets of edge boundary conditions. J Eng Math 2000;37(1):211–30.

[71] Narita Y, Ohta Y, Yamada G, Kobayashi Y. Analytical method for vibration of angle-ply cylindrical shells having arbitrary edges. AIAA J 1992;30(3):790–6.

[72] Olson MD, Fung Y. Comparing theory and experiment for the supersonic flutter of circular cylindrical shells. AIAA J 1967;5(10):1849–56.